

## Time-temperature superposition of polybutadiene vitrimers

Ralm G. Ricarte,<sup>1,\*</sup> Sachin Shanbhag,<sup>2,\*</sup> Dana Ezzeddine,<sup>1</sup> Daniel Barzycki,<sup>1</sup> and Kevin Fay<sup>1</sup>

<sup>1</sup>Department of Chemical and Biomedical Engineering, FAMU-FSU College of Engineering, Tallahassee, FL 32310 and <sup>2</sup>Department of Scientific Computing, Florida State University, Tallahassee, FL 32306

### Abstract

A vitrimer has covalent cross-links that preserve network connectivity but permit topology fluctuations through dynamic exchange reactions. In this work, we investigate the linear rheology of polybutadiene (PB) vitrimers bearing cross-links that exchange via dioxaborolane metathesis. PB vitrimers are cross-linked in solution using photoinitiated thiol-ene click chemistry. As the targeted cross-link density is increased, both the insoluble fraction and glass transition temperature increase. Linear viscoelasticity is studied using a combination of small amplitude oscillatory shear (SAOS), creep, and stress relaxation measurements. In SAOS, the elastic modulus is approximately constant while the viscous modulus increases as angular frequency decreases. In creep, the compliance displays power law behavior that persists for at least 8 hrs. In stress relaxation, the modulus transitions from a rubbery plateau into a power law regime. Both SAOS and creep data are visually superposed into master curves using horizontal shift factors that exhibit Arrhenius behavior. However, the activation energies of the SAOS shift factors ( $E_a^{SAOS}$ ) are smaller than those of the creep shift factors ( $E_a^{creep}$ ).  $E_a^{SAOS}$  matches the effective Williams-Landel-Ferry activation energy for PB homopolymer, indicating that the short time dynamics correspond to network strand segment relaxations. In contrast,  $E_a^{creep}$  is significantly larger than the activation energies predicted by established theoretical models for transient networks. We speculate that the discrepancy between experiment and theory is due to the temperature dependence of the cross-linker mobility within the vitrimer matrix, which is not fully captured by established theoretical models.

**Keywords:** Vitrimer, dynamic covalent polymer network, rheology

## Introduction

Dynamic covalent polymer networks – also known as transient networks, reversible networks, or covalent adaptable networks – contain cross-links between chains that exchange through a chemical reaction.<sup>1,2,3,4,5</sup> From a theoretical perspective, such networks were first modeled by Green and Tobolsky to rationalize the stress relaxation behavior of vulcanized rubbers. In their theory, stress decays exponentially and follows an Arrhenius-like relationship with temperature.<sup>6</sup> Flory, and later Fricker, considered similar systems in which cross-links within a network ruptured and reformed simultaneously, thereby preserving network connectivity but enabling network topology fluctuations. Based on both intuitive and mathematically rigorous arguments, they predicted that at long times stress relaxation exhibits a power law decay governed by the lifetime of a cross-link ( $\tau_{XL}$ ).<sup>7,8,9</sup> Baxandall and Leibler *et al.* separately developed reversible network theories that accounted for the primitive Rouse and reptation relaxations of network strands. According to these sticky Rouse and sticky reptation models, three distinct time regimes occur in stress relaxation: (I) an initial decay representative of Rouse motions, (II) a rubbery plateau whose modulus is proportional to the sum of the cross-link and entanglement densities, and (III) a terminal relaxation directly controlled by  $\tau_{XL}$ .<sup>10,11,12</sup> In this work, we study the different time regimes during relaxation of polybutadiene vitrimers, a class of dynamic covalent polymer networks that engage in *associative* exchange reactions.

Vitrimer cross-links exchange through an addition/elimination pathway, *i.e.*, a new covalent linkage between two chains is formed before an existing bond is fragmented. As a consequence, the network maintains connectivity and constant cross-link density, thereby preventing dissolution of polymer in good solvent at all temperatures below backbone degradation conditions. At the same time, however, cross-link exchange enables the network topology to fluctuate and the material to flow.<sup>2,3,4,5</sup> This combination of solvent resistance and processability makes vitrimers not only appealing for improving plastic sustainability and high-performance applications,<sup>13,14,15,16,17,18,19,20,21,22,23,24,25,26,27,28,29,30,31,32,33</sup> but also as a platform for investigating how dynamic cross-links impact the physics of the underlying polymer chains.

In particular, understanding vitrimer rheology has garnered significant interest, as their viscoelasticity regulates the efficiency of their processing and recycling. In the seminal works of Montarnal, Tournilhac, Leibler, and coworkers, epoxy vitrimers whose cross-links exchanged via a metal catalyzed transesterification had stress relaxation behavior that could be described by a monomodal exponential decay. The relaxation rate obeyed an Arrhenius relationship with temperature, with the apparent activation energy from rheology ( $E_a^{rh}$ ) being comparable to the activation energy for transesterification in small molecule analogues of the epoxy network ( $E_a^{sm}$ ).<sup>34,35,36</sup> As the vitrimer concept was translated to different backbone and cross-link chemistries, however, deviations from these simple trends were seen.  $E_a^{rh}$  values are usually much larger than the  $E_a^{sm}$ .<sup>15,20,37,38,39,40</sup> Broad non-exponential decays are commonly observed in stress relaxation.<sup>41,42,43,44,45,46,47,48,49,50</sup> The temperature dependence over a wide range cannot be described by a single activation energy.<sup>48,51,52,53,54</sup>

Responding to these observations, experimental, computational, and theoretical efforts over the past five years have focused on illuminating the relationship between vitrimer viscoelasticity and temperature. Generally, the relaxation rate expresses two different temperature regimes, where the estimated activation energy of the low temperature regime is less than that of the high temperature regime.<sup>48,51,53,49,55,56,57</sup> In 2021, Ricarte and Shanbhag used a generalized form of the sticky Rouse model to evaluate the role of backbone and cross-link chemistry on vitrimer viscoelasticity. At temperatures well above the glass transition, they observed that the short time

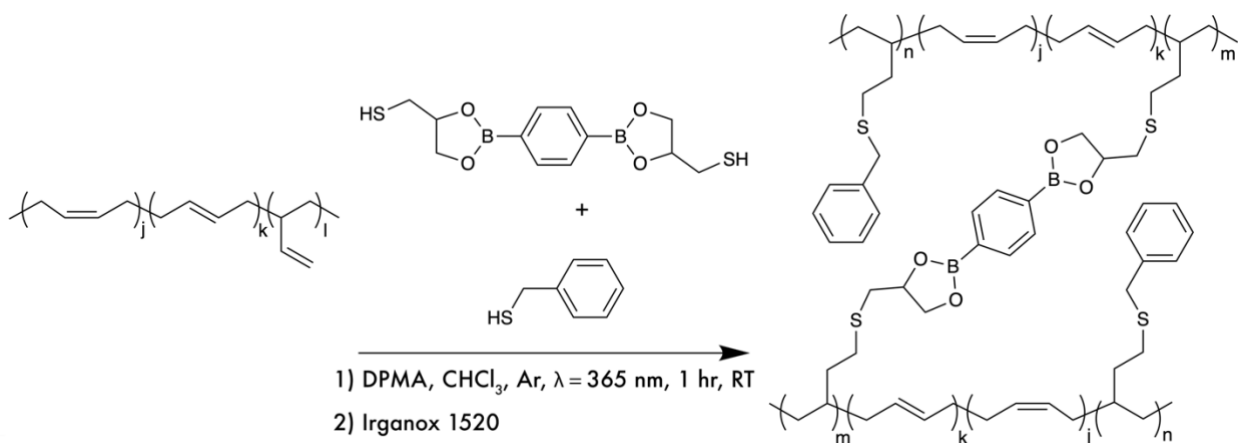
dynamics represented monomer friction. The activation energy associated with this time regime corresponded to an effective activation energy that could be calculated using the Williams-Landel-Ferry (WLF) parameters for the vitrimer backbone ( $E_a^{WLF}$ ). Conversely, the intermediate and terminal dynamics portrayed a combination of network strand relaxation and cross-link exchange. The resulting activation energy of this long time regime ( $E_a^{sticky}$ ) was estimated by the simple formula

$$E_a^{sticky} = E_a^{WLF} + E_a^{sm} \quad (1)$$

Due to the different activation energies of each regime, time-temperature superposition of the entire relaxation spectrum could not be achieved. However, the short and long time relaxation regimes were superposed using different sets of horizontal shift factors.<sup>58</sup>

Using our previous sticky Rouse modeling as a guide, in this work we investigate the thermorheological behavior of polybutadiene (PB) vitrimers bearing dioxaborolane cross-links (Scheme 1). The combination of a flexible polymer backbone and relatively slow cross-link exchange kinetics allows us to separate the short and long time relaxation dynamics. Furthermore, the  $E_a^{sm}$  for small molecule dioxaborolane metathesis has already been measured,<sup>15</sup> facilitating comparison of the activation energies from rheology. We probe the linear viscoelasticity of PB vitrimers with varying cross-link density using a combination of small-amplitude oscillatory shear (SAOS), creep, and stress relaxation measurements. At temperatures over 100 °C above the glass transition, PB vitrimers achieve power law behavior that persists for at least 8 hrs. SAOS and creep data are collapsed using different sets of horizontal shift factors ( $a_{SAOS}$  and  $a_{creep}$ ) that each follow Arrhenius temperature dependences. The activation energies associated with  $a_{SAOS}$  match the expected  $E_a^{WLF}$  values for PB homopolymer, suggesting that the short time dynamics correspond to PB segment relaxations. In contrast, the activation energies associated with  $a_{creep}$  are larger than the  $E_a^{sticky}$  values expected from Eqn. 1, especially at higher cross-link densities. We speculate that this discrepancy stems from the temperature dependence of the cross-link mobility within the PB matrix ( $\sigma$ ). Attempts to describe the  $\sigma$  temperature dependence using established microscopic models are discussed.

**Scheme 1.** Synthetic scheme for polybutadiene (PB) vitrimers.



## Materials and Methods

**Materials.** Polybutadiene ( $M_N = 6800$  g/mol,  $\bar{D} = 1.41$ , 1,2-addition = 12 mol%), benzyl mercaptan, 1,4-benzenedimethanethiol, 2,2-dimethoxy-2-phenylacetophenone, 1,2-octanediol, chloroform, and tetrahydrofuran were obtained from Sigma-Aldrich. Benzene-1,4-diboronic acid was obtained from Apollo Scientific. 2-methyl-4,6-bis[(*n*-octylthio)methyl]phenol (Irganox 1520) was obtained from TCI Chemicals. Magnesium sulfate was obtained from VWR.

**Size exclusion chromatography (SEC) of precursor polybutadiene (PB).** SEC of the precursor PB was performed using an Agilent-Wyatt combination triple detection SEC instrument equipped with three successive Agilent PL-gel Mixed C columns (25 °C THF mobile phase). The instrument also featured an Agilent 1260 infinity series pump, degasser, autosampler, and thermostatted column chamber. The triple detection unit consisted of a MiniDawn TREOS 3-angle light scattering detector, Optilab TrEX refractive index detector, and a Viscostart II differential viscometer. For determination of the absolute molar masses, a refractive index increment of 0.134 was used.<sup>59</sup>

**Synthesis of 2,2'-(1,4-Phenylene)-bis[4-thioethyl-1,3,2-dioxaborolane] (dioxaborolane cross-linker).** The synthesis of the dioxaborolane cross-linker was conducted based on the scheme reported in Breuillac *et al.*<sup>60</sup> Benzene-1,4-diboronic acid (10 g), 3-mercapto-1,2-propanediol (13.38 g), and tetrahydrofuran (100 mL) were combined in a roundbottom flask and stirred for five minutes. Magnesium sulfate (16.66 g) was added, and the mixture was stirred at room temperature for 48 hrs, filtered, and concentrated under reduced pressure. The remaining precipitate was dried under reduced pressure at 100 °C for 18 hrs to yield 16.9 g of a white powder (81% yield). Figure S5 is the <sup>1</sup>H NMR spectrum (600 MHz, CDCl<sub>3</sub>):  $\delta$  7.81 (s, 4H), 4.74 (q,  $J = 6.2$  Hz, 2H), 4.50 (m, 2H), 4.17 (m, 2H), 2.81 (m, 4H), 1.48 (t,  $J = 8.6$  HZ, 2H). Figure S6 is the <sup>13</sup>C NMR spectrum (600 MHz, CDCl<sub>3</sub>):  $\delta$  134.3, 77.7, 70.0, 29.8. The carbon adjacent to the boron was not detected.

**PB vitrimer synthesis.** PB vitrimers were prepared using photoinitiated thiol-ene click chemistry. The polymer backbone was functionalized using a mixture of dioxaborolane cross-linker and benzyl mercaptan. Varying the ratio of dioxaborolane cross-linker to benzyl mercaptan allowed the cross-link density to be tuned while maintaining a constant amount of sulfide and aromatic groups within the sample. Table 1 lists the sample names, and targeted number of dioxaborolane cross-links and benzyl mercaptan groups. Samples are named as PB- $\nu$ - $N_{XL}$ , where  $N_{XL}$  is the targeted number of dioxaborolane cross-links per polybutadiene chain.

**Table 1.** PB vitrimer targeted number of cross-links ( $N_{XL}$ ) and benzyl mercaptan groups ( $N_{BM}$ ) per PB chain. For all samples, the targeted number of sulfides per PB chain  $N_{sulfide} = N_{XL} + N_{BM} = 15$ .

Sample ID	$N_{XL}$	$N_{BM}$
PB- $\nu$ -1	1	14
PB- $\nu$ -4	4	11
PB- $\nu$ -8	8	7
PB- $\nu$ -15	15	0

Scheme 1 outlines the synthetic procedure for PB vitrimers. To prepare PB-*v*-4, polybutadiene (1.00 g, 2.2 mmol of vinyl groups), dioxaborolane cross-linker (0.09516 g, 0.275 mmol), benzyl mercaptan (0.2049 g, 1.65 g), 2,2-dimethoxy-2-phenylacetophenone (0.0575 g, 0.22 mmol), and dry chloroform (4.8 mL) were mixed in a scintillation vial, transferred into a 10 mL cylindrical single neck Schlenk flask, and degassed through three freeze-pump-thaw cycles. Cross-linking was performed by exposing the reaction mixture to UV light (MelodySusie Model DR-301Z,  $\lambda = 365$  nm, Flux = 800  $\mu\text{W}/\text{cm}^2$ ) for 1 hr. After UV exposure, the resulting gel was doped with 0.1 mL of a solution containing 0.002 g of Irganox 1520 dissolved in dry chloroform, and then stored in the dark at ambient temperature for 24 hrs. The gel was then transferred to a scintillation vial and dried under reduced pressure at 75 °C for 18 hrs to yield 1.13 g of a translucent solid.

**Thermal characterization.** Differential scanning calorimetry was performed using a TA Instruments DSC Q2000. 4 – 5 mg of sample were placed inside an aluminum pan with a standard lid. Under a nitrogen gas flow of 50 mL/min, PB vitrimers samples were first cooled from 0 to – 80 °C, heated to 180 °C, cooled to – 80 °C, and finally reheated to 180 °C. All heating and cooling rates had a magnitude of 10 °C/min. The glass transition temperature ( $T_g$ ) was measured from the inflection point in the second heating trace. All samples were examined by DSC in triplicate.

**Insoluble fraction measurement.** The insoluble content of PB vitrimer samples was quantified using the method of Röttger *et al.*<sup>15</sup> 0.1 g of sample was placed inside a stainless steel fine wire cage and submerged in 40 g of dried chloroform. After 24 h, the cage was removed from the solvent and dried under reduced pressure at 75 °C for at least 18 hr. The mass of the remaining insoluble portion of the vitrimer was measured to determine the insoluble fraction. The sample remaining in the cage was then resubmerged in a chloroform solution containing an excess of 1,2-octanediol. The addition of the diol caused each of the vitrimer samples to fully dissolve, confirming the absence of nondynamic static cross-links in the PB vitrimer networks.

**Rheology measurements.** Linear viscoelasticity of PB vitrimers was evaluated using an Anton Paar MCR 302e rotational rheometer equipped with parallel plate geometry. The upper geometry was an 8 mm aluminum disposable plate, while the lower geometry was a 25 mm stainless steel plate with Peltier temperature control. To minimize sample slip, both upper and lower plates had profiled surfaces. To minimize thermal degradation, the plate geometry was encased in a hood under a 200 L/hr nitrogen flow. The geometry achieved a temperature control accuracy of  $\pm 0.1$  °C. During measurements, a normal force between 0.1 to 1 N was applied to maintain contact between the sample and upper plate. PB vitrimer samples were molded into disc shapes (8 mm diameter and 1.5 mm thickness) using stainless steel frames, which were subjected to an applied load of 3 tons at 150 °C for 8 min.

Strain amplitude sweeps, small-amplitude oscillatory shear (SAOS), stress relaxation, and creep compliance and recovery measurements were conducted. From the strain amplitude sweeps (Figure S12), a linear viscoelastic regime was identified at temperatures of 100 and 180 °C. For SAOS and stress relaxation, measurements on fresh samples at all temperatures were performed at an imposed strain value that was within both the linear viscoelastic regimes identified at 100 and 180 °C (see Table S2). To improve reproducibility of results, samples were subjected to a pre-conditioning routine prior to SAOS, stress relaxation, and creep measurements. The pre-

conditioning routine is detailed in the Supporting Information. SAOS measurements were run at angular frequencies ( $\omega$ ) ranging from 100 to 0.01 rad/s. Stress relaxation measurements were run for 8 hrs. Creep compliance and recovery measurements were run for 8 and 2 hrs, respectively.

Time-temperature superposition was performed on SAOS, creep compliance, and stress relaxation data using a reference temperature  $T_R = 120$  °C. Vertical shift factors for SAOS ( $b_{SAOS}$ ) were calculated by

$$b_{SAOS}(T) = \frac{G'_p(T_R)}{G'_p(T)} \quad (2)$$

where  $G'_p(T)$  and  $G'_p(T_R)$  are the magnitude of the elastic modulus plateau at temperature  $T$  and  $T_R$ , respectively. After applying  $b_{SAOS}$ , horizontal shift factors for SAOS measurements ( $a_{SAOS}$ ) were determined by manually superposing the  $\tan \delta$  data. Vertical shift factors for creep and stress relaxation measurements ( $b_{creep}$  and  $b_{stress}$ ) were determined by

$$b_{stress}(T) = \frac{G_p(T_R)}{G_p(T)} \quad (3)$$

$$b_{creep}(T) = \frac{J_p(T)}{J_p(T_R)} \quad (4)$$

where  $G_p(T)$  and  $G_p(T_R)$  are the stress relaxation plateau moduli at  $T$  and  $T_R$ , while  $J_p(T)$  and  $J_p(T_R)$  are the instantaneous compliances at  $T$  and  $T_R$ .<sup>61</sup> Plateau moduli from stress relaxation and instantaneous compliances from creep were calculated by averaging the data between 0.1 to 10 s. After applying  $b_{creep}$ , horizontal shift factors for creep measurements ( $a_{creep}$ ) were determined by manually superposing the compliance data.

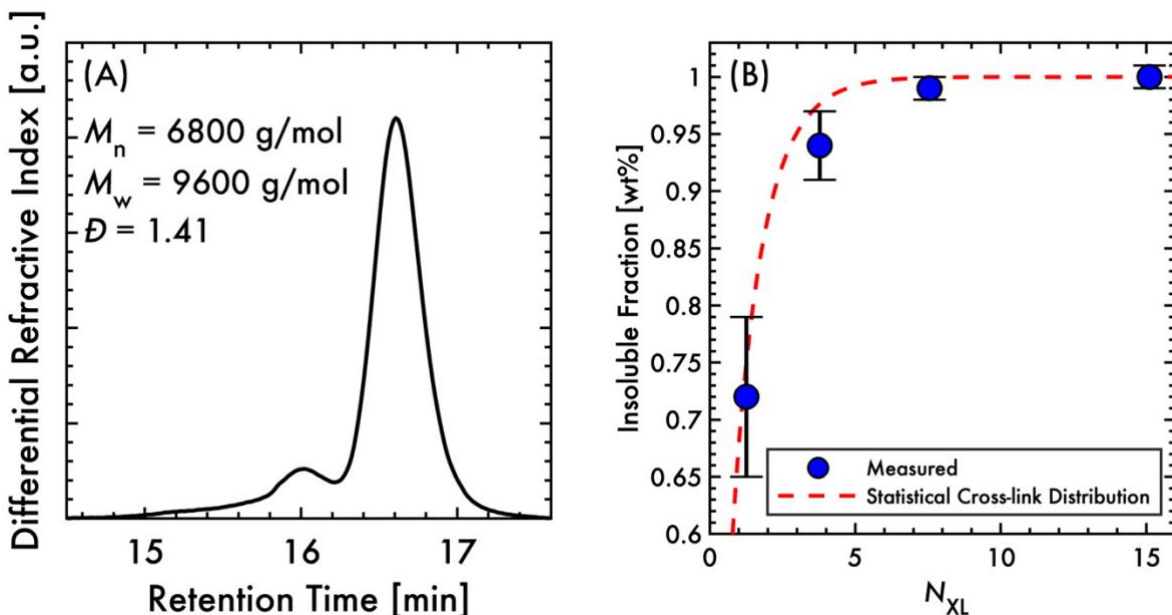
Portions of PB vitrimer samples used for rheology were subject to extraction in chloroform in the presence of excess 1,2-octanediol. All samples completely dissolved, suggesting that the material did not form a static cross-linked network during the rheological measurements.

## Results

**PB vitrimer characterization.** PB vitrimers bearing dioxaborolane cross-links were prepared using photoinitiated thiol-ene click chemistry. The cross-links engage in a dioxaborolane metathesis exchange reaction, which has an activation energy  $E_a^{sm} = 15.1$  kJ/mol. These cross-links are able to exchange without the need of an external catalyst.<sup>3,15</sup> The synthesis and rheology of a static cross-link PB thermoset control sample are described in the Supporting Information.

Table 1 details the targeted number of dioxaborolane cross-links and pendant benzyl mercaptan groups per PB chain ( $N_{XL}$  and  $N_{BM}$ , respectively) of the vitrimer samples. While both  $N_{XL}$  and  $N_{BM}$  are varied, their sum – corresponding to the targeted number of sulfide bonds per PB chain ( $N_S$ ) – is kept constant. The samples featured in this work are labeled as PB- $v$ - $N_{XL}$ . Infrared spectroscopy, thermal gravimetric analysis, differential scanning calorimetry, and small-angle X-ray scattering (SAXS) are detailed in the Supporting Information.

Figure 1A illustrates the SEC trace of the precursor PB. The peak at 16 min is attributed to the presence of branched chains. Additional characterization of the precursor PB is featured in the Supporting Information.



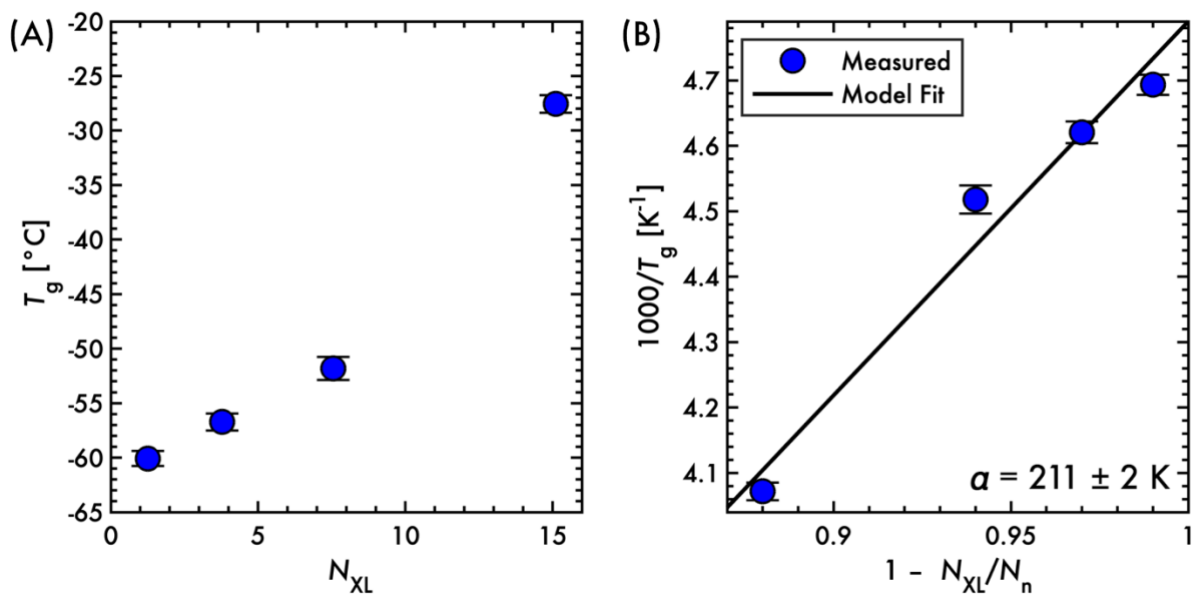
**Figure 1.** (A) Precursor PB SEC trace. (B) PB vitrimer insoluble fraction vs. targeted number of cross-links per PB chain ( $N_{XL}$ ). Error bars represent the standard deviation of triplicate measurements.

Figure 1B depicts the insoluble fraction of the PB vitrimers as a function of  $N_{XL}$ . The measured insoluble fractions, which increase as  $N_{XL}$  increases, are compared to the expected values. The dashed red curve is the estimated weight fraction of chains bearing at least 1 dioxaborolane cross-link, as calculated using Eqn. S3. This line essentially represents the maximum possible insoluble fraction for a system with statistically distributed *nondynamic* cross-links and the same molar mass distribution as the precursor PB. The measured insoluble fractions match this limit. Along with the featureless scattering patterns observed by SAXS (Figure S11), the agreement between the measured and expected insoluble fractions suggest that the PB vitrimers are not macro- or microphase separated.

Figure 2A plots the glass transition temperature ( $T_g$ ) vs.  $N_{XL}$ . During differential scanning calorimetry measurements, only a single  $T_g$  is observed between  $-80$  to  $180$  °C (Figure S10). The measured  $T_g$ , which increases as  $N_{XL}$  increases, can be described using

$$\frac{1}{T_g} = \frac{1}{\alpha} \left( 1 - \frac{N_{XL}}{N_n} \right) \quad (5)$$

where  $\alpha = 211 \pm 2$  K is an empirical constant determined from using a linear regression. Figure 2B fits Eqn. 5 to the measured  $T_g$  values.



**Figure 2.** (A) Glass transition temperature  $T_g$  vs.  $N_{XL}$ . Error bars represent standard deviation of triplicate measurements. (B) Eqn. 5 fit to  $T_g$  data. Error bars represent propagated error.

**Linear viscoelasticity.** Figures 3A, S14A, S15A, and S16A depict SAOS measurements. For all samples, the elastic modulus ( $G'$ ) is approximately constant over the range of angular frequencies ( $\omega$ ) from 0.01 to 100 rad/s. The magnitude of  $G'$  increases with  $N_{XL}$  (Figure S21). In contrast, the viscous modulus ( $G''$ ) increases as  $\omega$  decreases. The magnitude of the  $G''$  rise increases as temperature increases.  $\tan \delta$  curves, featured in Figure S17, depict similar trends.

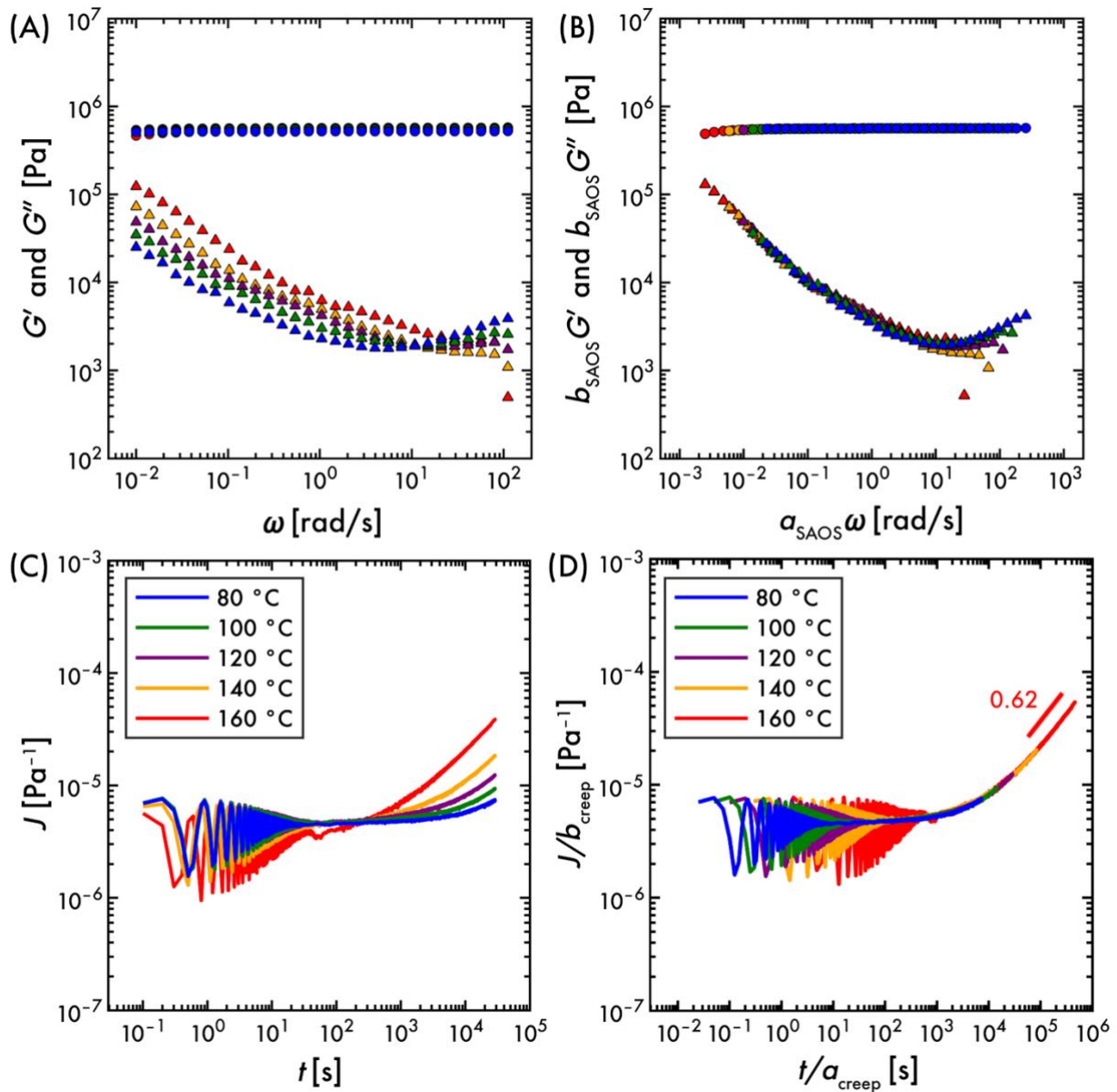


**Figure 3.** Linear viscoelastic measurements of PB-v-4. (A) SAOS as measured and (B) with  $a_{SAOS}$  horizontal shift factors applied. (C) Creep as measured and (D) with  $a_{creep}$  horizontal shift factors applied. Reference temperature for both  $a_{SAOS}$  and  $a_{creep}$  is 120 °C.

Figures 3C, S14C, S15C, and S16C detail creep measurements. Prior to 100 s, the creep compliance ( $J$ ) exhibits a dampening sinusoidal response, typical of elastic materials.<sup>62,63</sup> After 100 s,  $J$  increases and adopts a power law relationship with time.  $J$  rises more significantly as temperature is increased. The power law scaling exponent for  $J$ , however, is much lower than the characteristic steady state flow scaling of 1, even after a period of 24 hrs (Figure S26). Similarly, the creep recovery compliance ( $J_{rec}$ ) increases over time but does not reach a plateau over a period of 2 hrs (Figure S19). The magnitude of  $J_{rec}$  increases as both temperature and  $N_{XL}$  increase.

Figures 3B and 3D are SAOS and creep master curves for PB-v-4. Master curves for the other samples are listed in the Supporting Information. Superposition of the data was performed

by applying both vertical and horizontal shift factors. The horizontal shift factors for SAOS and creep are labeled as  $a_{SAOS}$  and  $a_{creep}$ , respectively. For SAOS,  $G'$  and  $G''$  data below  $a_{SAOS} \omega = 10$  rad/s collapse into a single curve. Likewise, the  $J$  data after  $\frac{t}{a_{creep}} = 10^3$  s superpose into a single curve.

Figures 4 and S20 plot  $a_{SAOS}$  and  $a_{creep}$  versus inverse temperature. Although both  $a_{SAOS}$  and  $a_{creep}$  show an approximate Arrhenius dependence,  $a_{creep}$  has a stronger temperature sensitivity. Activation energies  $E_a^{SAOS}$  and  $E_a^{creep}$  are calculated by fitting the following equations to the horizontal shift factors

$$\ln(a_{SAOS}) = \frac{E_a^{SAOS}}{R} \left( \frac{1}{T} - \frac{1}{T_R} \right) + \text{intercept} \quad (6)$$

$$\ln(a_{creep}) = \frac{E_a^{creep}}{R} \left( \frac{1}{T} - \frac{1}{T_R} \right) + \text{intercept} \quad (7)$$

where  $T$  is temperature,  $T_R$  is the reference temperature of 393.15 K, and  $R$  is the gas constant. For all samples,  $E_a^{creep} > E_a^{SAOS} > E_a^{sm} = 15.1$  kJ/mol.<sup>15</sup>

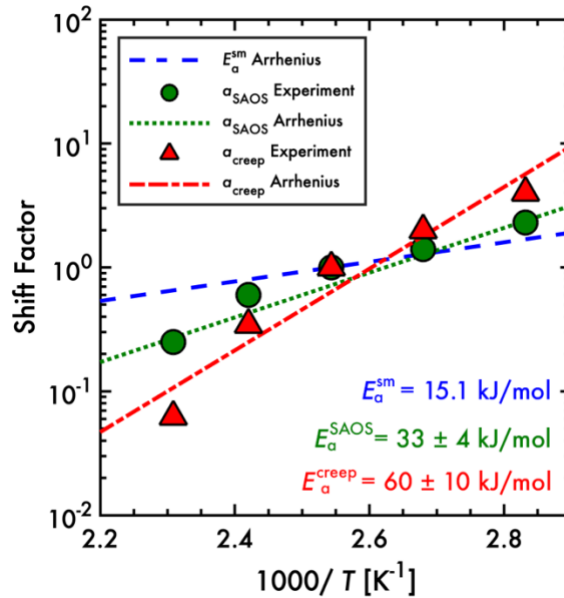


**Figure 4.** Arrhenius fits of  $a_{SAOS}$  and  $a_{creep}$  horizontal shift factors for PB-v-4. Reference temperature for both  $a_{SAOS}$  and  $a_{creep}$  is 393.15 K.

Figures 5, S23, S24, and S25 illustrate stress relaxation measurements. At early times, the stress relaxation modulus ( $G$ ) sits on a plateau. The magnitude of this plateau modulus increases with  $N_{XL}$  (Figure S21). After  $\approx 100$  s,  $G$  exhibits a relaxation whose rate increases with temperature. Eventually,  $G$  displays apparent power law behavior at longer times. Although the

low signal-to-noise ratio of the long time data inhibit determination of horizontal shift factors from stress relaxation experiments, application of  $a_{SAOS}$  and  $a_{creep}$  shift factors demonstrate that the  $G$  data do not obey time temperature superposition over the entire time range. Application of  $a_{SAOS}$  causes  $G$  to overlap at  $\frac{t}{a_{SAOS}} \approx 10^3$  s. Application of  $a_{creep}$  causes the apparent power law portion of the  $G$  curves to superpose. For PB- $\nu$ -1 and PB- $\nu$ -4, power law exponents of approximately  $-1/2$  are identified. For PB- $\nu$ -8 and PB- $\nu$ -15, the low signal-to-noise ratio of the 160 °C data prevents precise determination of a power law scaling.

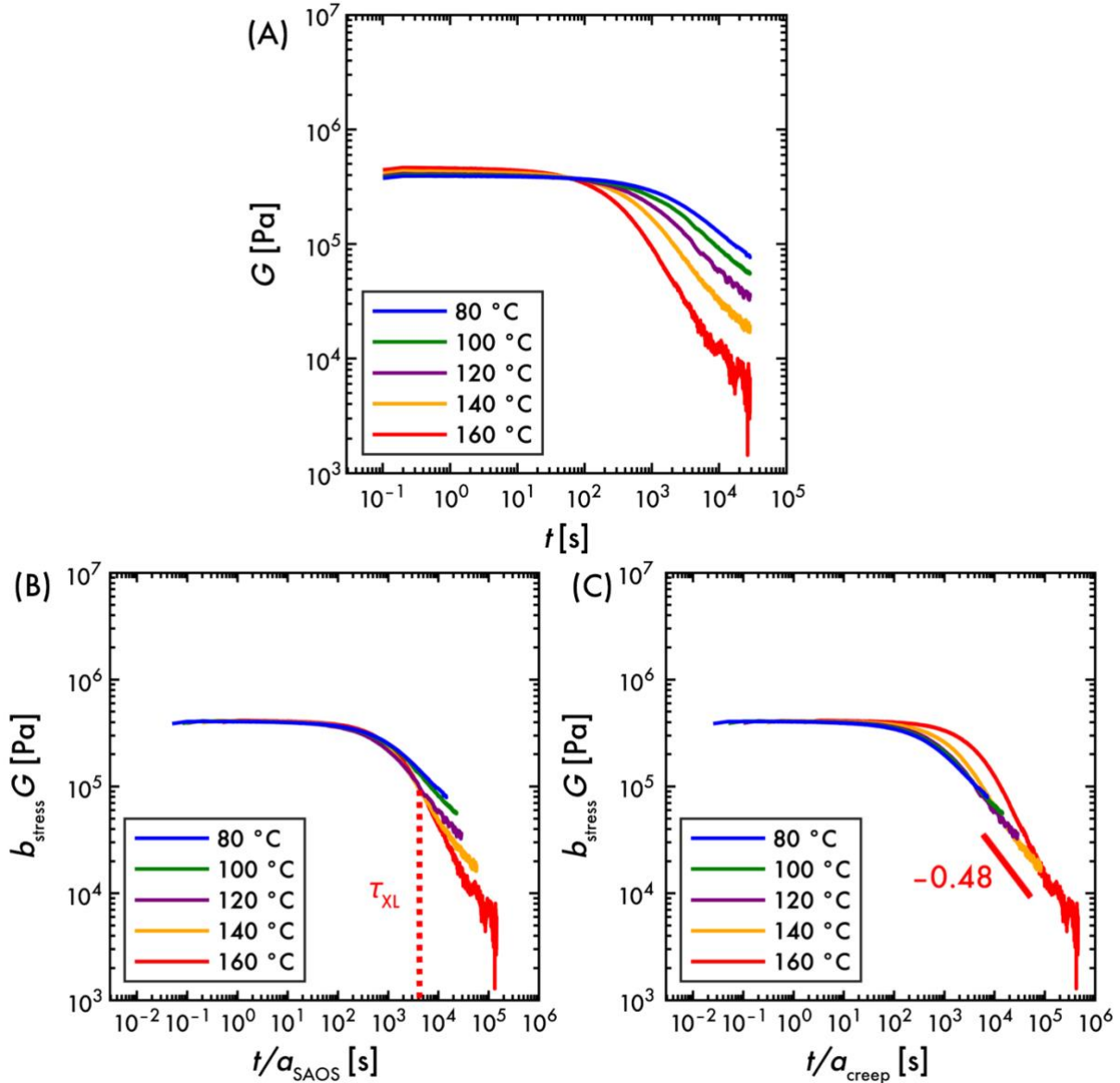


**Figure 5.** Stress relaxation of PB- $\nu$ -4 (A) as measured, (B) with  $a_{SAOS}$ , and (C)  $a_{creep}$  horizontal shift factors applied. In (B), dashed line represents cross-link lifetime ( $\tau_{XL}$ ) estimated from the Prony series analysis. Reference temperature for both  $a_{SAOS}$  and  $a_{creep}$  is 120 °C.

**Activation Energies.** Figure 6 plots  $E_a^{SAOS}$  and  $E_a^{creep}$  versus  $T_g$ . The  $E_a^{SAOS}$  data are compared to the following  $E_a^{WLF}$  model

$$E_a^{WLF} = \frac{2.303C_1C_2T_R^2}{(C_2 + T_R - T_g - 55 \text{ K})^2} \quad (8)$$

where  $T_g$  is the glass transition temperature measured from DSC,  $T_R = 393.15 \text{ K}$  is the reference temperature, and  $C_1$  and  $C_2$  are the WLF parameters for PB homopolymer (see Supporting Information for derivation). Not only are the measured  $E_a^{SAOS}$  consistent with the rheological activation energy of the precursor PB (Figure S4C), they also quantitatively match the expected  $E_a^{WLF}$  values estimated using Eqn. 8.  $E_a^{creep}$  data are compared to the overall activation energy predicted by the sticky Rouse and sticky reptation theories ( $E_a^{sticky}$ , Eqn. 1). At low  $N_{XL}$  and  $T_g$ ,  $E_a^{creep}$  is comparable to  $E_a^{sticky}$ . As  $N_{XL}$  and  $T_g$  increase, however, the discrepancy between  $E_a^{creep}$  and  $E_a^{sticky}$  grows larger.

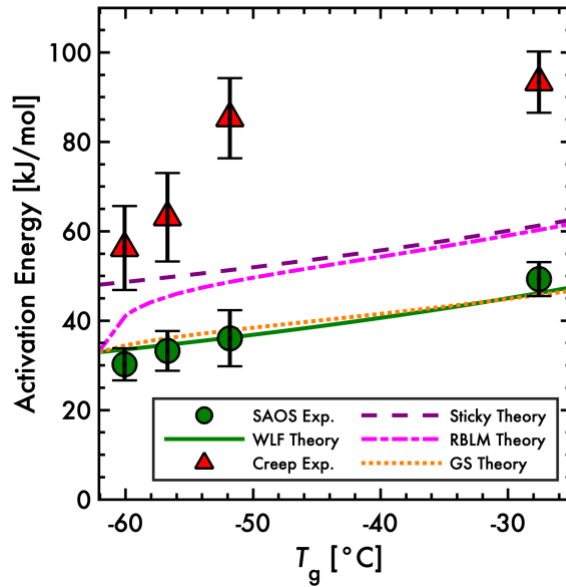


**Figure 6.** Comparison of measured activation energies from SAOS and creep vs. WLF, sticky Rouse and sticky reptation (Sticky), renormalized bond lifetime (RBLM), and Ghosh-Schweizer (GS) models. Reference temperature for all activation energies is 393.15 K. Error bars represent the standard error from the Arrhenius fits.

**Summary of linear viscoelasticity results.** SAOS, creep, and stress relaxation measurements were performed on PB vitrimers with varying cross-link density. Both SAOS and creep data exhibit approximate Arrhenius relationships with temperature, but the resulting horizontal shift factors

have different activation energies.  $E_a^{SAOS}$  is consistent with predictions from the WLF theory, while  $E_a^{creep}$  grows to be much larger than the predictions from sticky Rouse and sticky reptation theories.

## Discussion

In the linear viscoelastic regime, PB vitrimers exhibit relaxations that are not observed for the static cross-link PB thermoset control sample (Figure S27). For many vitrimer systems, time-temperature superposition is successful at collapsing viscoelastic data that occur during the initial transition from the rubbery plateau regime to longer time relaxations. In SAOS, for instance, this corresponds to the region surrounding the  $G'$ - $G''$  crossover frequency ( $\omega_{cross}$ ). For measurements collected over wide time or frequency ranges, however, the short and long time dynamics do not superpose into a single master curve.<sup>39,51,53,54</sup> As evidenced by the different shift factors for SAOS and creep experiments in this study, the thermorheological behavior of PB vitrimers agrees with these trends.

The PB vitrimer  $G'$  and  $G''$  only capture the dynamic response of the rubbery plateau regime. According to the framework of the sticky Rouse and sticky reptation models, this describes the time period between the Rouse decay of the glassy modes and the first instance of cross-link exchange ( $\tau_{XL} = \frac{1}{\omega_{cross}}$ ).<sup>11</sup> The agreement between the measured  $E_a^{SAOS}$  and predicted  $E_a^{WLF}$  strongly suggests that the observed upturn in  $G''$  represents segmental motions of the PB network strands. As this behavior occurs at frequencies above  $\omega_{cross}$ , we propose that subdiffusive segmental motions facilitate cross-link exchange events. This concept is consistent with previous theoretical arguments regarding reactive polymer systems.<sup>64,65,66,67,68,69,70,71,72,73</sup>

For the long time dynamics, the interpretation is much more complex. The beginning of this regime is signaled by  $\tau_{XL}$  (or, equivalently,  $\omega_{cross}$ ). Although, we do not directly capture the  $G'$ - $G''$  crossover in our SAOS data, we can roughly approximate it by fitting the stress relaxation modulus to an empirical Prony series, and then using the fitting parameters to extrapolate  $G'$  and  $G''$  to lower angular frequencies (see Supporting Information). As an example, for PB- $\nu$ -4 at 120 °C we estimate  $\tau_{XL} \approx 4000$  s, which coincides with the time point in which time-temperature superposition begins to fail in the stress relaxation master curve depicted in Figure 5B. The origin of the lengthy power law regime is less clear. For stress relaxation, the sticky Rouse model anticipates an intermediate relaxation regime in which  $G \sim t^{-\frac{1}{2}}$ .<sup>11,12,58,74,75,76,77,78</sup> Hybrid Monte Carlo-molecular dynamics simulations by Perego and Khabaz also detected intermediate regimes of  $G \sim t^{-\frac{1}{2}}$  in stress relaxation and  $J \sim t^{\frac{1}{2}}$  in creep.<sup>53</sup> This intermediate regime is expected to last until a terminal relaxation time ( $\tau_1$ ) is reached. While sticky Rouse theory expects that  $\tau_1 \sim \tau_{XL} N_{XL}^2$ ,<sup>58</sup> we do not observe any indication of terminal relaxation in our rheological measurements, even for PB- $\nu$ -1. Moreover, the transient network model of Fricker actually associates terminal relaxation with a  $G \sim t^{-\frac{1}{2}}$  scaling.<sup>8,9</sup> Without directly observing  $\tau_1$ , we cannot precisely assign the measured long time dynamics to a particular relaxation regime.

For the temperature dependence of the long time dynamics, the measured  $E_a^{creep}$  and predicted  $E_a^{sticky}$  diverge as  $N_{XL}$  and, consequently,  $T_g$  increase. This relationship is similar to the trend Hajj *et al.* observed for the activation energy of vitrimer networks bearing imine cross-links.<sup>40</sup> We suspect that the discrepancy between  $E_a^{creep}$  and  $E_a^{sticky}$  potentially arises from an assumption in our previous work.<sup>58</sup> There, we described  $\tau_{XL}$  using

$$\tau_{XL} = \sigma \tau_0 \exp\left(\frac{E_a^{sm}}{RT}\right) \quad (9)$$

where  $R$  is the gas constant,  $T$  is temperature, and  $\tau_0$  is the elementary Rouse timescale.  $\sigma$  is a parameter that portrays the mobility of the associative cross-links within the vitrimer matrix.  $E_a^{sticky}$  is defined as

$$E_a^{sticky} = \frac{\partial}{\partial\left(\frac{1}{RT}\right)} \ln \tau_{XL} = \frac{\partial}{\partial\left(\frac{1}{RT}\right)} \ln \sigma + \frac{\partial}{\partial\left(\frac{1}{RT}\right)} \ln \tau_0 + \frac{\partial}{\partial\left(\frac{1}{RT}\right)} \frac{E_a^{sm}}{RT} \quad (10)$$

$$E_a^{sticky} = \frac{\partial}{\partial\left(\frac{1}{RT}\right)} \ln \sigma + E_a^{WLF} + E_a^{sm} \quad (11)$$

$$E_a^{WLF} = \frac{\partial}{\partial\left(\frac{1}{RT}\right)} \ln \tau_0 \quad (12)$$

In our prior work, we assumed that  $\sigma$  was independent of temperature, causing the first derivative term in Eqn. 11 to cancel and resulting in the form of  $E_a^{sticky}$  described in Eqn. 1. Relaxing that assumption creates an additional contribution to  $E_a^{sticky}$

$$E_a^{sticky} = \frac{\partial}{\partial\left(\frac{1}{RT}\right)} \ln \sigma + E_a^{WLF} + E_a^{sm} = E_a^\sigma + E_a^{WLF} + E_a^{sm} \quad (13)$$

For this reason, we speculate that the larger than expected values for  $E_a^{creep}$  originate from the temperature dependence of  $\sigma$ .

Although we introduced the  $\sigma$  parameter in our previous work,<sup>58</sup> the relationship between cross-link mobility and  $\tau_{XL}$  has already been studied through the lens of microscopic theories, albeit mostly for networks with *dissociative* cross-links that rearrange via an elimination/addition pathway.<sup>3,68,73</sup> For the Renormalized Bond Lifetime Model (RBLM) of Rubinstein and Semenov,  $\tau_{XL}$  accounts for both the subdiffusive motions of backbone repeat units and cross-link re-associations that do not contribute to stress relaxation.<sup>68,72</sup> We derive explicit expressions for the cross-link mobility and long time dynamics activation energy ( $\sigma^{RBLM}$  and  $E_a^{RBLM}$ , respectively) using the RBLM framework and assuming the cross-links undergo Rouse-like subdiffusive motion

$$\sigma^{RBLM} = Z \left( 1 + Z^3 \exp\left(-\frac{E_a^{sm}}{RT}\right) \right) \quad (14)$$

$$E_a^{RBLM} = E_a^{WLF} + \frac{E_a^{sm}}{1 + Z^3 \exp\left(-\frac{E_a^{sm}}{RT}\right)} \quad (15)$$

where  $Z$  is the number of times a cross-linkable group reassociates with an old partner (see Supporting Information for derivation). Another transient network theory is the model of Ghosh and Schweizer (GS), in which local frictional resistance of the backbone segments attenuates the overall temperature dependence of the network relaxation.<sup>54,79</sup> Combining the RBLM and GS models, we can develop alternative forms of the cross-link mobility and long time dynamics activation energy ( $\sigma^{GS}$  and  $E_a^{GS}$ )

$$\sigma^{GS} = Z \left( \left( \frac{\tau_0}{\tau} \right)^{\nu-1} + (1 + Z^3) \exp \left( - \frac{E_a^{sm}}{RT} \right) \right) \quad (16)$$

$$E_a^{GS} = E_a^{WLF} + \frac{\tau_0^{\nu-1} E_a^{sm} + (\nu - 1) E_a^{WLF}}{1 + \frac{1 + Z^3}{\tau^{1-\nu} \tau_0^{\nu-1} \exp \left( \frac{E_a^{sm}}{RT} \right)}} \quad (17)$$

where  $\nu$  is a decoupling exponent and  $\tau$  is the elementary attempt time for activated relaxation.<sup>79</sup>

While Eqns. 15 and 17 provide elegantly simple forms for the activation energies, they do not accurately describe our experimental data. The second terms in each expression essentially diminish the influence of  $E_a^{sm}$ , leading to weaker temperature dependences relative to  $E_a^{sticky}$ . Consequently, both  $E_a^{RBLM}$  and  $E_a^{GS}$  also severely underestimate the measured  $E_a^{creep}$ . Thus, the discrepancy between the expected and measured values of  $E_a^{creep}$  becomes larger after incorporating the temperature dependence of cross-link mobility as modeled in established theories.

## Conclusion

The linear viscoelasticity of PB vitrimers with varying dioxaborolane cross-link density was evaluated using a combination of SAOS, creep, and stress relaxation. The short and long time dynamics exhibit different temperature dependences, preventing complete superposition of the stress relaxation curves at varying temperatures well above  $T_g$ . The activation energy of the short time dynamics is consistent with monomer friction of the PB backbone, suggesting that segmental motions precipitate the initial cross-link exchange events. The long time dynamics, characterized by prolonged power law regimes in stress relaxation and creep measurements, express an activation energy that is larger than the predicted values of the sticky Rouse and sticky reptation models.

We speculate that the discrepancy between the measured  $E_a^{creep}$  and predicted  $E_a^{sticky}$  values originates from the temperature dependence of the cross-link mobility within the PB backbone matrix,  $\sigma$ . Theories that describe cross-linker subdiffusion, such as the RBLM and GS models, have been successfully used to describe the dynamics of polymer networks with dissociative cross-links. For PB vitrimers with associative cross-links, however, we find that they are unable to resolve the discrepancy between  $E_a^{creep}$  and  $E_a^{sticky}$ . In fact, modeling cross-linker subdiffusion using these theories exacerbates the disagreement between the measured and theoretical activation energy estimates.

Our findings identify a knowledge gap in understanding the mechanism of associative cross-link exchange within a vitrimer system. To resolve this open question, we propose investigating vitrimer rheology using a framework centered around the role of the cross-link

mobility  $\sigma$ . Developing a molecular description of  $\sigma$  for vitrimers will not only clarify the features of the linear viscoelastic response, but also the dynamics under larger strains and stresses. Knowledge of the latter regime is of particular importance for optimizing the flow behavior during extrusion, injection, 3D printing, and other standard forms of polymer processing.<sup>24,63,80</sup> Moving forward, the combination of experiment, computations, and theory will be needed to illuminate the impact of molecular structure on vitrimer dynamics.

### **Author information**

#### *Corresponding Authors*

Ralm G. Ricarte

\*E-mail: rricarte@eng.famu.fsu.edu

Sachin Shanbhag

\*E-mail: sshanbhag@fsu.edu

#### *ORCID*

Ralm G. Ricarte: 0000-0003-1018-6083

Sachin Shanbhag: 0000-0002-7807-112X

Dana Ezzeddine: 0000-0003-1633-3953

Daniel C. Barzycki: 0000-0001-8067-0087

Kevin Fay: 0009-0008-3421-4804

### **Acknowledgements**

We are very grateful to Dr. Rufina Alamo and the Alamo Laboratory for use of their differential scanning calorimeter. We are very grateful to Dr. Rebekah Sweat and the Sweat Laboratory for use of their rheometer for measurements on the precursor PB. We are very grateful to Dr. Subramanian Ramakrishnan and the Ramakrishnan Laboratory for use of their rheometer for conducting preliminary measurements. We are very grateful to Dr. Justin Kennemur and the Kennemur Laboratory for use of their size-exclusion chromatography instrument. We are very grateful to the Florida State University High-Performance Materials Institute for use of their characterization equipment. We are very grateful to the Florida State University Department of Chemistry and Biochemistry for use of the Nuclear Magnetic Resonance Spectroscopy Facility. We thank Dr. Stephanie Marxsen, Guanrui Li, Jaehoon Jang, and Zachary Bauer for help with experiments. This research used resources of the Advanced Photon Source, a U.S. Department of Energy (DOE) Office of Science User Facility operated for the DOE Office of Science by Argonne National Laboratory under Contract DE-AC02-06CH11357. We thank Steven Weigand of the Advanced Photon Source for his help in using beamline DND-CAT 5ID-D. This work was supported primarily by the National Science Foundation (DMR-2144007). This work was partially supported by funds provided by the Oak Ridge Associated Universities Foundation, ORAU-Directed Research and Development Program. This work is based in part upon work supported by the National Science Foundation under grant no. NSF DMR-1727870. This work was also supported using start-up funds from Florida State University and the Florida A&M – Florida State University College of Engineering.

## Supporting Information

Characterization of precursor polybutadiene,  $^1\text{H}$  and  $^{13}\text{C}$  nuclear magnetic resonance spectroscopy of dioxaborolane cross-linker, PB vitrimer attenuated total reflectance infrared spectroscopy, PB vitrimer thermal characterization, PB vitrimer small-angle X-ray scattering, estimated insoluble fraction for networks with a statistical cross-link distribution, PB vitrimer strain amplitude sweeps, parameters for rheological measurements, preconditioning procedure for rheological measurements, SAOS and creep data for PB- $\nu$ -1, PB- $\nu$ -8, and PB- $\nu$ -15,  $\tan \delta$  data, creep recovery compliance data,  $a_{SAOS}$  and  $a_{creep}$  shift factors for PB- $\nu$ -1, PB- $\nu$ -8, and PB- $\nu$ -15, plateau moduli and vertical shift factors, stress relaxation for PB- $\nu$ -1, PB- $\nu$ -8, and PB- $\nu$ -15, 24 hr creep of PB- $\nu$ -15, static cross-link PB thermoset synthesis and SAOS, creep, and stress relaxation, Prony series analysis for PB- $\nu$ -4, and derivation of  $E_a^{WLF}$ ,  $\sigma^{RBLM}$ ,  $E_a^{RBLM}$ ,  $\sigma^{GS}$ , and  $E_a^{GS}$  models.

## References

- <sup>1</sup>Kloxin, C. J.; Bowman, C. N. Covalent Adaptable Networks: Smart, Reconfigurable and Responsive Network Systems. *Chem Soc Rev* **2013**, *42*, 7161–7173. <https://doi.org/10.1039/c3cs60046g>.
- <sup>2</sup>Scheutz, G. M.; Lessard, J. J.; Sims, M. B.; Sumerlin, B. S. Adaptable Crosslinks in Polymeric Materials: Resolving the Intersection of Thermoplastics and Thermosets. *J Am Chem Soc* **2019**, *141*, 16181–16196. <https://doi.org/10.1021/jacs.9b07922>.
- <sup>3</sup>Winne, J. M.; Leibler, L.; Prez, F. E. D. Dynamic Covalent Chemistry in Polymer Networks: A Mechanistic Perspective. *Polym Chem* **2019**, *10*, 6091–6108. <https://doi.org/10.1039/c9py01260e>.
- <sup>4</sup>Zee, N. J. V.; Nicolaÿ, R. Vitrimers: Permanently Crosslinked Polymers with Dynamic Network Topology. *Prog Polym Sci* **2020**, *104*, 101233. <https://doi.org/10.1016/j.progpolymsci.2020.101233>.
- <sup>5</sup>Porath, L.; Soman, B.; Jing, B. B.; Evans, C. M. Vitrimers: Using Dynamic Associative Bonds to Control Viscoelasticity, Assembly, and Functionality in Polymer Networks. *ACS Macro Lett* **2022**, *11*, 475–483. <https://doi.org/10.1021/acsmacrolett.2c00038>.
- <sup>6</sup>Green, M. S.; Tobolsky, A. V. A New Approach to the Theory of Relaxing Polymeric Media. *J Chem Phys* **1946**, *14*, 80–92. <https://doi.org/10.1063/1.1724109>.
- <sup>7</sup>Flory, P. J. Elasticity of Polymer Networks Cross-Linked in States of Strain. *Trans Faraday Soc* **1960**, *56*, 722–743. <https://doi.org/10.1039/tf9605600722>.
- <sup>8</sup>Fricker, H. S. The Effects on Rubber Elasticity of the Addition and Scission of Cross-Links under Strain. *Proc Royal Soc Lond Math Phys Sci* **1973**, *335*, 267–287. <https://doi.org/10.1098/rspa.1973.0125>.
- <sup>9</sup>Fricker, H. S. On the Theory of Stress Relaxation by Cross-Link Reorganization. *Proc Royal Soc Lond Math Phys Sci* **1973**, *335*, 289–300. <https://doi.org/10.1098/rspa.1973.0126>.
- <sup>10</sup>Baxandall, L. G. Dynamics of Reversibly Crosslinked Chains. *Macromolecules* **1989**, *22*, 1982–1988. <https://doi.org/10.1021/ma00194a076>.
- <sup>11</sup>Leibler, L.; Rubinstein, M.; Colby, R. H. Dynamics of Reversible Networks. *Macromolecules* **1991**, *24*, 4701–4707. <https://doi.org/10.1021/ma00016a034>.
- <sup>12</sup>Leibler, L.; Rubinstein, M.; Colby, R. H. Dynamics of Telechelic Ionomers. Can Polymers Diffuse Large Distances without Relaxing Stress? *J Phys II* **1993**, *3*, 1581–1590. <https://doi.org/10.1051/jp2:1993219>.

- <sup>13</sup>Chabert, E.; Vial, J.; Cauchois, J.-P.; Mihaluta, M.; Tournilhac, F. Multiple Welding of Long Fiber Epoxy Vitrimer Composites. *Soft Matter* **2016**, *12*, 4838–4845. <https://doi.org/10.1039/c6sm00257a>.
- <sup>14</sup>Imbernon, L.; Norvez, S. From Landfilling to Vitrimer Chemistry in Rubber Life Cycle. *Eur Polym J* **2016**, *82*, 347–376. <https://doi.org/10.1016/j.eurpolymj.2016.03.016>.
- <sup>15</sup>Röttger, M.; Domenech, T.; Weegen, R. van der; Breuillac, A.; Nicolaÿ, R.; Leibler, L. High-Performance Vitrimers from Commodity Thermoplastics through Dioxaborolane Metathesis. *Science* **2017**, *356*, 62–65. <https://doi.org/10.1126/science.aah5281>.
- <sup>16</sup>Demongeot, A.; Groote, R.; Goossens, H.; Hoeks, T.; Tournilhac, F.; Leibler, L. Cross-Linking of Poly(Butylene Terephthalate) by Reactive Extrusion Using Zn(II) Epoxy-Vitrimer Chemistry. *Macromolecules* **2017**, *50*, 6117–6127. <https://doi.org/10.1021/acs.macromol.7b01141>.
- <sup>17</sup>Shi, Q.; Yu, K.; Kuang, X.; Mu, X.; Dunn, C. K.; Dunn, M. L.; Wang, T.; Qi, H. J. Recyclable 3D Printing of Vitrimer Epoxy. *Mater Horizons* **2017**, *4*, 598–607. <https://doi.org/10.1039/c7mh00043j>.
- <sup>18</sup>Jing, B. B.; Evans, C. M. Catalyst-Free Dynamic Networks for Recyclable, Self-Healing Solid Polymer Electrolytes. *J Am Chem Soc* **2019**, *141*, 18932–18937. <https://doi.org/10.1021/jacs.9b09811>.
- <sup>19</sup>Lee, J.; Jing, B. B.; Porath, L. E.; Sottos, N. R.; Evans, C. M. Shock Wave Energy Dissipation in Catalyst-Free Poly(Dimethylsiloxane) Vitrimers. *Macromolecules* **2020**, *53*, 4741–4747. <https://doi.org/10.1021/acs.macromol.0c00784>.
- <sup>20</sup>Lessard, J. J.; Scheutz, G. M.; Hughes, R. W.; Sumerlin, B. S. Polystyrene-Based Vitrimers: Inexpensive and Recyclable Thermosets. *ACS Appl Polym Mater* **2020**, *2*, 3044–3048. <https://doi.org/10.1021/acsapm.0c00523>.
- <sup>21</sup>Lv, G.; Soman, B.; Shan, N.; Evans, C. M.; Cahill, D. G. Effect of Linker Length and Temperature on the Thermal Conductivity of Ethylene Dynamic Networks. *ACS Macro Lett* **2021**, *10*, 1088–1093. <https://doi.org/10.1021/acsmacrolett.1c00423>.
- <sup>22</sup>Ma, J.; Porath, L. E.; Haque, M. F.; Sett, S.; Rabbi, K. F.; Nam, S.; Miljkovic, N.; Evans, C. M. Ultra-Thin Self-Healing Vitrimer Coatings for Durable Hydrophobicity. *Nat Commun* **2021**, *12*, 5210. <https://doi.org/10.1038/s41467-021-25508-4>.
- <sup>23</sup>Farge, L.; Hoppe, S.; Daujat, V.; Tournilhac, F.; André, S. Solid Rheological Properties of PBT-Based Vitrimers. *Macromolecules* **2021**, *54*, 1838–1849. <https://doi.org/10.1021/acs.macromol.0c02105>.

- <sup>24</sup>Kim, S.; Rahman, M. A.; Arifuzzaman, M.; Gilmer, D. B.; Li, B.; Wilt, J. K.; Lara-Curzio, E.; Saito, T. Closed-Loop Additive Manufacturing of Upcycled Commodity Plastic through Dynamic Cross-Linking. *Sci Adv* **2022**, *8*, eabn6006. <https://doi.org/10.1126/sciadv.abn6006>.
- <sup>25</sup>Debsharma, T.; Amfilochiou, V.; Wróblewska, A. A.; Baere, I. D.; Paepegem, W. V.; Prez, F. E. D. Fast Dynamic Siloxane Exchange Mechanism for Reshapable Vitriimer Composites. *J Am Chem Soc* **2022**, *144*, 12280–12289. <https://doi.org/10.1021/jacs.2c03518>.
- <sup>26</sup>Fang, H.; Gao, X.; Zhang, F.; Zhou, W.; Qi, G.; Song, K.; Cheng, S.; Ding, Y.; Winter, H. H. Triblock Elastomeric Vitrimers: Preparation, Morphology, Rheology, and Applications. *Macromolecules* **2022**. <https://doi.org/10.1021/acs.macromol.2c01711>.
- <sup>27</sup>Chappuis, S.; Edera, P.; Cloitre, M.; Tournilhac, F. Enriching an Exchangeable Network with One of Its Components: The Key to High-T<sub>g</sub> Epoxy Vitrimers with Accelerated Relaxation. *Macromolecules* **2022**, *55*, 6982–6991. <https://doi.org/10.1021/acs.macromol.2c01005>.
- <sup>28</sup>Langenbach, J.; Bakkali-Hassani, C.; Poutrel, Q.-A.; Georgopoulou, A.; Clemens, F.; Tournilhac, F.; Norvez, S. Adhesion and Stiffness Matching in Epoxy-Vitrimers/Strain Sensor Fiber Laminates. *ACS Appl Polym Mater* **2022**, *4*, 1264–1275. <https://doi.org/10.1021/acsapm.1c01648>.
- <sup>29</sup>Lijsebetten, F. V.; Engelen, S.; Bauters, E.; Vooren, W. V.; Smulders, M. M. J.; Prez, F. E. D. Recyclable Vitriimer Epoxy Coatings for Durable Protection. *Eur Polym J* **2022**, *176*, 111426. <https://doi.org/10.1016/j.eurpolymj.2022.111426>.
- <sup>30</sup>Lv, G.; Li, X.; Jensen, E.; Soman, B.; Tsao, Y.-H.; Evans, C. M.; Cahill, D. G. Dynamic Covalent Bonds in Vitrimers Enable 1.0 W/(m K) Intrinsic Thermal Conductivity. *Macromolecules* **2023**. <https://doi.org/10.1021/acs.macromol.2c02264>.
- <sup>31</sup>Fabrizio, L.; Arrigo, R.; Scrivani, M. T.; Monti, M.; Fina, A. Upcycling of PET from Recycled Food Packaging Trays via Vitrimers Chemistry. *Polymer* **2023**, *266*, 125618. <https://doi.org/10.1016/j.polymer.2022.125618>.
- <sup>32</sup>Bakkali-Hassani, C.; Edera, P.; Langenbach, J.; Poutrel, Q.-A.; Norvez, S.; Gresil, M.; Tournilhac, F. Epoxy Vitriimer Materials by Lipase-Catalyzed Network Formation and Exchange Reactions. *ACS Macro Lett* **2023**, 338–343. <https://doi.org/10.1021/acsmacrolett.2c00715>.
- <sup>33</sup>Stewart, K. A.; DeLellis, D. P.; Lessard, J. J.; Rynk, J. F.; Sumerlin, B. S. Dynamic Ablative Networks: Shapeable Heat-Shielding Materials. *ACS Appl Mater Inter* **2023**. <https://doi.org/10.1021/acsami.2c22924>.
- <sup>34</sup>Montarnal, D.; Capelot, M.; Tournilhac, F.; Leibler, L. Silica-Like Malleable Materials from Permanent Organic Networks. *Science* **2011**, *334*, 965–968. <https://doi.org/10.1126/science.1212648>.

- <sup>35</sup>Capelot, M.; Unterlass, M. M.; Tournilhac, F.; Leibler, L. Catalytic Control of the Vitrimer Glass Transition. *ACS Macro Lett* **2012**, *1*, 789–792. <https://doi.org/10.1021/mz300239f>.
- <sup>36</sup>Capelot, M.; Montarnal, D.; Tournilhac, F.; Leibler, L. Metal-Catalyzed Transesterification for Healing and Assembling of Thermosets. *J Am Chem Soc* **2012**, *134*, 7664–7667. <https://doi.org/10.1021/ja302894k>.
- <sup>37</sup>Nishimura, Y.; Chung, J.; Muradyan, H.; Guan, Z. Silyl Ether as a Robust and Thermally Stable Dynamic Covalent Motif for Malleable Polymer Design. *J Am Chem Soc* **2017**, *139*, 14881–14884. <https://doi.org/10.1021/jacs.7b08826>.
- <sup>38</sup>Lessard, J. J.; Garcia, L. F.; Easterling, C. P.; Sims, M. B.; Bentz, K. C.; Arencibia, S.; Savin, D. A.; Sumerlin, B. S. Catalyst-Free Vitrimers from Vinyl Polymers. *Macromolecules* **2019**, *52*, 2105–2111. <https://doi.org/10.1021/acs.macromol.8b02477>.
- <sup>39</sup>Spießschaert, Y.; Taplan, C.; Stricker, L.; Guerre, M.; Winne, J. M.; Prez, F. E. D. Influence of the Polymer Matrix on the Viscoelastic Behaviour of Vitrimers. *Polym Chem* **2020**, *11*, 5377–5385. <https://doi.org/10.1039/d0py00114g>.
- <sup>40</sup>Hajj, R.; Duval, A.; Dhers, S.; Avérous, L. Network Design to Control Polyimine Vitrimer Properties: Physical Versus Chemical Approach. *Macromolecules* **2020**, *53*, 3796–3805. <https://doi.org/10.1021/acs.macromol.0c00453>.
- <sup>41</sup>Meng, F.; Pritchard, R. H.; Terentjev, E. M. Stress Relaxation, Dynamics, and Plasticity of Transient Polymer Networks. *Macromolecules* **2016**, *49*, 2843–2852. <https://doi.org/10.1021/acs.macromol.5b02667>.
- <sup>42</sup>Li, L.; Chen, X.; Jin, K.; Torkelson, J. M. Vitrimers Designed Both To Strongly Suppress Creep and To Recover Original Cross-Link Density after Reprocessing: Quantitative Theory and Experiments. *Macromolecules* **2018**, *51*, 5537–5546. <https://doi.org/10.1021/acs.macromol.8b00922>.
- <sup>43</sup>Meng, F.; Saed, M. O.; Terentjev, E. M. Elasticity and Relaxation in Full and Partial Vitrimer Networks. *Macromolecules* **2019**, *52*, 7423–7429. <https://doi.org/10.1021/acs.macromol.9b01123>.
- <sup>44</sup>El-Zaatari, B. M.; Ishibashi, J. S. A.; Kalow, J. A. Cross-Linker Control of Vitrimer Flow. *Polym Chem* **2020**, *11*, 5339–5345. <https://doi.org/10.1039/d0py00233j>.
- <sup>45</sup>Saed, M. O.; Gablier, A.; Terentjev, E. M. Liquid Crystalline Vitrimers with Full or Partial Boronic-Ester Bond Exchange. *Adv. Funct. Mater.* **2020**, *30*, 1906458. <https://doi.org/10.1002/adfm.201906458>.

- <sup>46</sup>Song, Z.; Wang, Z.; Cai, S. Mechanics of Vitrimer with Hybrid Networks. *Mech Mater* **2021**, *153*, 103687. <https://doi.org/10.1016/j.mechmat.2020.103687>.
- <sup>47</sup>Anaya, O.; Jourdain, A.; Antoniuk, I.; Romdhane, H. B.; Montarnal, D.; Drockenmuller, E. Tuning the Viscosity Profiles of High- $T_g$  Poly(1,2,3-Triazolium) Covalent Adaptable Networks by the Chemical Structure of the N-Substituents. *Macromolecules* **2021**, *54*, 3281–3292. <https://doi.org/10.1021/acs.macromol.0c02221>.
- <sup>48</sup>Porath, L. E.; Evans, C. M. Importance of Broad Temperature Windows and Multiple Rheological Approaches for Probing Viscoelasticity and Entropic Elasticity in Vitrimers. *Macromolecules* **2021**, *54*, 4782–4791. <https://doi.org/10.1021/acs.macromol.0c02800>.
- <sup>49</sup>Porath, L.; Huang, J.; Ramlawi, N.; Derkaloustian, M.; Ewoldt, R. H.; Evans, C. M. Relaxation of Vitrimers with Kinetically Distinct Mixed Dynamic Bonds. *Macromolecules* **2022**, *55*, 4450–4458. <https://doi.org/10.1021/acs.macromol.1c02613>.
- <sup>50</sup>Xu, H.; Wang, H.; Zhang, Y.; Wu, J. Vinylogous Urethane Based Epoxy Vitrimers with Closed-Loop and Multiple Recycling Routes. *Ind Eng Chem Res* **2022**, *61*, 17524–17533. <https://doi.org/10.1021/acs.iecr.2c03393>.
- <sup>51</sup>Guerre, M.; Taplan, C.; Nicolaÿ, R.; Winne, J. M.; Prez, F. E. D. Fluorinated Vitrimer Elastomers with a Dual Temperature Response. *J Am Chem Soc* **2018**, *140*, 13272–13284. <https://doi.org/10.1021/jacs.8b07094>.
- <sup>52</sup>Meng, F.; Saed, M. O.; Terentjev, E. M. Rheology of Vitrimers. *Nat Commun* **2022**, *13*, 5753. <https://doi.org/10.1038/s41467-022-33321-w>.
- <sup>53</sup>Perego, A.; Lazarenko, D.; Cloitre, M.; Khabaz, F. Microscopic Dynamics and Viscoelasticity of Vitrimers. *Macromolecules* **2022**, *55*, 7605–7613. <https://doi.org/10.1021/acs.macromol.2c00588>.
- <sup>54</sup>Soman, B.; Schweizer, K. S.; Evans, C. M. Fragile Glass Formation and Non-Arrhenius Upturns in Ethylene Vitrimers Revealed by Dielectric Spectroscopy. *Macromolecules* **2022**, *56*, 166–176. <https://doi.org/10.1021/acs.macromol.2c01657>.
- <sup>55</sup>Jourdain, A.; Asbai, R.; Anaya, O.; Chehimi, M. M.; Drockenmuller, E.; Montarnal, D. Rheological Properties of Covalent Adaptable Networks with 1,2,3-Triazolium Cross-Links: The Missing Link between Vitrimers and Dissociative Networks. *Macromolecules* **2020**, *53*, 1884–1900. <https://doi.org/10.1021/acs.macromol.9b02204>.
- <sup>56</sup>Wu, S.; Yang, H.; Huang, S.; Chen, Q. Relationship between Reaction Kinetics and Chain Dynamics of Vitrimers Based on Dioxaborolane Metathesis. *Macromolecules* **2020**, *53*, 1180–1190. <https://doi.org/10.1021/acs.macromol.9b02162>.

<sup>57</sup>Wu, S.; Yang, H.; Xu, W.-S.; Chen, Q. Thermodynamics and Reaction Kinetics of Symmetric Vitrimers Based on Dioxaborolane Metathesis. *Macromolecules* **2021**, *54*, 6799–6809. <https://doi.org/10.1021/acs.macromol.1c00697>.

<sup>58</sup>Ricarte, R. G.; Shanbhag, S. Unentangled Vitriimer Melts: Interplay between Chain Relaxation and Cross-Link Exchange Controls Linear Rheology. *Macromolecules* **2021**, *54*, 3304–3320. <https://doi.org/10.1021/acs.macromol.0c02530>.

<sup>59</sup>Huang, S.; Han, L.; Ma, H.; Lei, L.; Zhang, R.; Shen, H.; Yang, L.; Li, C.; Zhang, S.; Li, Y. Determination of Refractive Index Increment of Synthetic Polybutadienes and Microstructural Control of Grafting Density and Liquid Crystalline Properties. *Polym Chem* **2020**, *11*, 2559–2567. <https://doi.org/10.1039/d0py00050g>.

<sup>60</sup>Breuillac, A.; Kassalias, A.; Nicolaÿ, R. Polybutadiene Vitrimers Based on Dioxaborolane Chemistry and Dual Networks with Static and Dynamic Cross-Links. *Macromolecules* **2019**, *52*, 7102–7113. <https://doi.org/10.1021/acs.macromol.9b01288>.

<sup>61</sup>Ferry, J. Viscoelastic Properties of Polymers, 3<sup>rd</sup> ed.; John Wiley & Sons Inc, 1980.

<sup>62</sup>Ewoldt, R. H.; McKinley, G. H. Creep Ringing in Rheometry or How to Deal with Oft-Discarded Data in Step Stress Tests! *Rheol. Bull.* **2007**, *76*.

<sup>63</sup>Ricarte, R. G.; Tournilhac, F.; Cloître, M.; Leibler, L. Linear Viscoelasticity and Flow of Self-Assembled Vitrimers: The Case of a Polyethylene/Dioxaborolane System. *Macromolecules* **2020**, *53*, 1852–1866. <https://doi.org/10.1021/acs.macromol.9b02415>.

<sup>64</sup>Gennes, P. G. de. Kinetics of Diffusion-controlled Processes in Dense Polymer Systems. I. Nonentangled Regimes. *J Chem Phys* **1982**, *76*, 3316–3321. <https://doi.org/10.1063/1.443328>.

<sup>65</sup>Gennes, P. G. de. Kinetics of Diffusion-controlled Processes in Dense Polymer Systems. II. Effects of Entanglements. *J Chem Phys* **1982**, *76*, 3322–3326. <https://doi.org/10.1063/1.443329>.

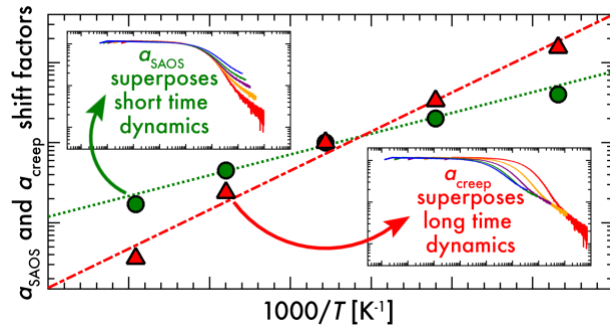
<sup>66</sup>Friedman, B.; O’Shaughnessy, B. Kinetics of Intermolecular Reactions in Dilute Polymer Solutions and Unentangled Melts. *Macromolecules* **1993**, *26*, 5726–5739. <https://doi.org/10.1021/ma00073a030>.

<sup>67</sup>Semenov, A. N.; Rubinstein, M. Thermoreversible Gelation in Solutions of Associative Polymers. 1. Statics. *Macromolecules* **1998**, *31*, 1373–1385. <https://doi.org/10.1021/ma970616h>.

<sup>68</sup>Rubinstein, M.; Semenov, A. N. Thermoreversible Gelation in Solutions of Associating Polymers. 2. Linear Dynamics. *Macromolecules* **1998**, *31*, 1386–1397. <https://doi.org/10.1021/ma970617+>.

- <sup>69</sup>Semenov, A. N.; Rubinstein, M. Dynamics of Strongly Entangled Polymer Systems: Activated Reptation. *European Phys J B - Condens Matter Complex Syst* **1998**, *1*, 87–94. <https://doi.org/10.1007/s100510050155>.
- <sup>70</sup>Rubinstein, M.; Semenov, A. N. Dynamics of Entangled Solutions of Associating Polymers. *Macromolecules* **2001**, *34*, 1058–1068. <https://doi.org/10.1021/ma0013049>.
- <sup>71</sup>Semenov, A. N.; Rubinstein, M. Dynamics of Entangled Associating Polymers with Large Aggregates. *Macromolecules* **2002**, *35*, 4821–4837. <https://doi.org/10.1021/ma0117965>.
- <sup>72</sup>Stukalin, E. B.; Cai, L.-H.; Kumar, N. A.; Leibler, L.; Rubinstein, M. Self-Healing of Unentangled Polymer Networks with Reversible Bonds. *Macromolecules* **2013**, *46*, 7525–7541. <https://doi.org/10.1021/ma401111n>.
- <sup>73</sup>Shanbhag, S.; Ricarte, R. G. On the Effective Lifetime of Reversible Bonds in Transient Networks. *Macromol Theory Simul* **2023**. <https://doi.org/10.1002/mats.202300002>.
- <sup>74</sup>Chen, Q.; Colby, R. H. Linear Viscoelasticity of Sulfonated Styrene Oligomers near the Sol-Gel Transition. *Korea-Aust Rheol J* **2014**, *26*, 257–261. <https://doi.org/10.1007/s13367-014-0030-4>.
- <sup>75</sup>Zhang, Z.; Chen, Q.; Colby, R. H. Dynamics of Associative Polymers. *Soft Matter* **2018**, *14*, 2961–2977. <https://doi.org/10.1039/c8sm00044a>.
- <sup>76</sup>Chen, Q. Dynamics in Miscible Polymer Blends and Associative Polymers. *Nihon Reoroji Gakk* **2019**, *47*, 197–205. <https://doi.org/10.1678/rheology.47.197>.
- <sup>77</sup>Yang, H.; Wu, S.; Chen, Q. Linear Viscoelasticity of Double Associative Polymers with Varied Density of the Secondary Interaction. *J Rheol* **2022**, *66*, 1113–1123. <https://doi.org/10.1122/8.0000394>.
- <sup>78</sup>Wu, S.; Chen, Q. Advances and New Opportunities in the Rheology of Physically and Chemically Reversible Polymers. *Macromolecules* **2022**, *55*, 697–714. <https://doi.org/10.1021/acs.macromol.1c01605>.
- <sup>79</sup>Ghosh, A.; Schweizer, K. S. Physical Bond Breaking in Associating Copolymer Liquids. *ACS Macro Lett* **2021**, *10*, 122–128. <https://doi.org/10.1021/acsmacrolett.0c00697>.
- <sup>80</sup>Ricarte, R. G.; Tournilhac, F.; Leibler, L. Phase Separation and Self-Assembly in Vitrimers: Hierarchical Morphology of Molten and Semicrystalline Polyethylene/Dioxaborolane Maleimide Systems. *Macromolecules* **2019**, *52*, 432–443. <https://doi.org/10.1021/acs.macromol.8b02144>.

# Table of Contents Image



Supporting Information for

**Time-temperature superposition of polybutadiene vitrimers**

Ralm G. Ricarte,<sup>1,\*</sup> Sachin Shanbhag,<sup>2,\*</sup> Dana Ezzeddine,<sup>1</sup> Daniel Barzycki,<sup>1</sup> and Kevin Fay<sup>1</sup>

<sup>1</sup>Department of Chemical and Biomedical Engineering, FAMU-FSU College of Engineering, Tallahassee, FL 32310 and <sup>2</sup>Department of Scientific Computing, Florida State University, Tallahassee, FL 32306

Email: [rricarte@eng.famu.fsu.edu](mailto:rricarte@eng.famu.fsu.edu) and [sshanbhag@fsu.edu](mailto:sshanbhag@fsu.edu)

**Table of Contents**

Characterization of precursor polybutadiene	S2
<sup>1</sup> H and <sup>13</sup> C nuclear magnetic resonance spectroscopy of dioxaborolane cross-linker	S6
PB vitrimer attenuated total reflectance infrared spectroscopy	S8
PB vitrimer thermal characterization	S9
PB vitrimer small-angle X-ray scattering	S10
Estimated insoluble fraction for networks with a statistical cross-link distribution	S11
PB vitrimer strain amplitude sweeps	S12
Parameters for rheological measurements	S13
Preconditioning procedure for rheological measurements	S13
SAOS and creep data for PB- $\nu$ -1, PB- $\nu$ -8, and PB- $\nu$ -15	S14
$\tan \delta$ data	S17
Creep recovery compliance data	S19
$a_{SAOS}$ and $a_{creep}$ shift factors for PB- $\nu$ -1, PB- $\nu$ -8, and PB- $\nu$ -15	S20
Plateau moduli and vertical shift factors	S21
Stress relaxation for PB- $\nu$ -1, PB- $\nu$ -8, and PB- $\nu$ -15	S23
24 hr creep of PB- $\nu$ -15	S26
Static cross-link PB thermoset synthesis and SAOS, creep, and stress relaxation	S26
Prony series analysis for PB- $\nu$ -4.	S28
Derivation of $E_a^{WLF}$ , $\sigma^{RBLM}$ , $E_a^{RBLM}$ , $\sigma^{GS}$ , and $E_a^{GS}$ models	S29
References	S33

### Characterization of precursor polybutadiene

$^1\text{H}$  nuclear magnetic resonance (NMR) spectroscopy was conducted using a Bruker Advance III 600 MHz NMR spectrometer.

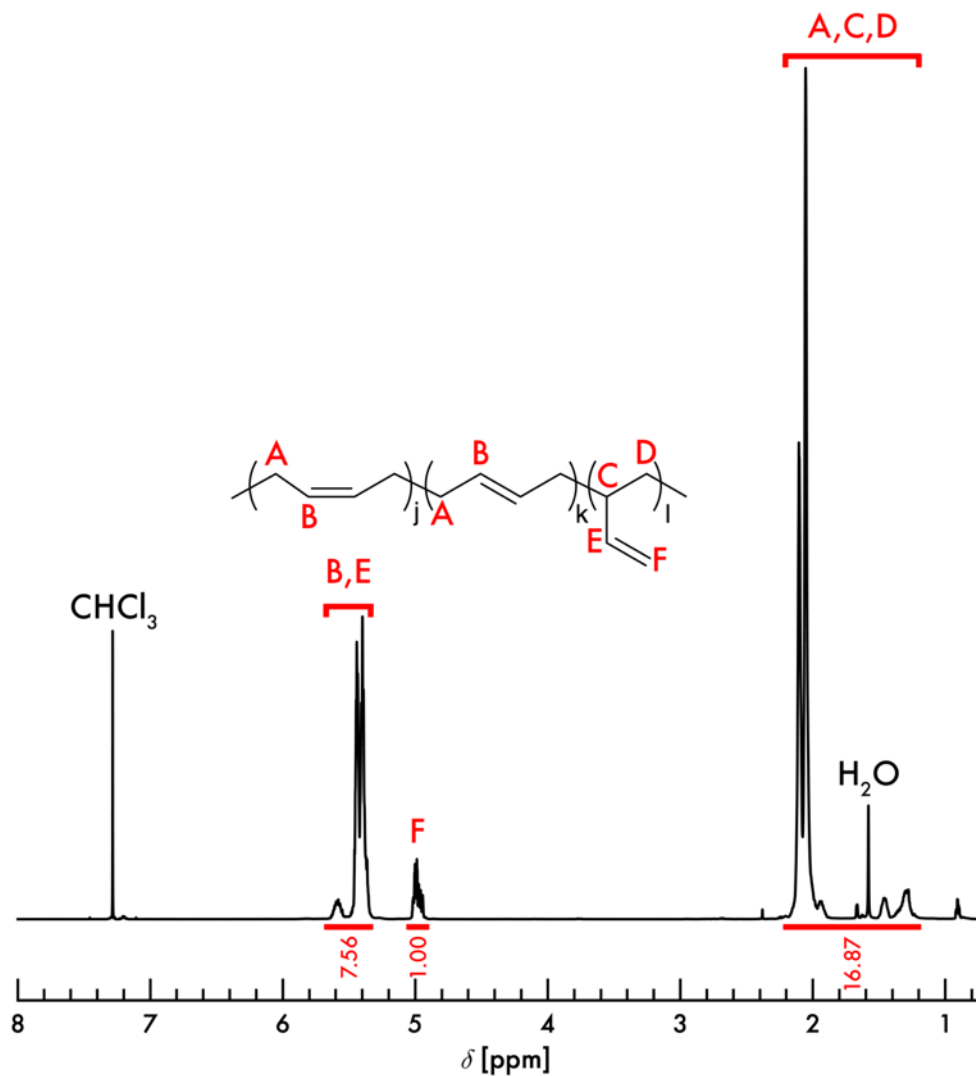


**Figure S1.** Precursor polybutadiene  $^1\text{H}$  NMR spectrum in  $\text{CDCl}_3$ .

PB attenuated total reflectance infrared spectroscopy (ATR-IR) spectra were collected using a Nicolet iS50 Fourier Transform Infrared Spectrometer equipped with a Smart iTR Attenuated Total Reflectance Sampling Accessory. The PB backbone displays signals at 1440 ( $\text{CH}_2$  bending), 1650 ( $\text{C}=\text{C}$  stretching), 2849 and 2917 ( $\text{CH}_2$  stretching), and  $3050\text{ cm}^{-1}$  ( $=\text{C}-\text{H}$  stretching).<sup>S1</sup>

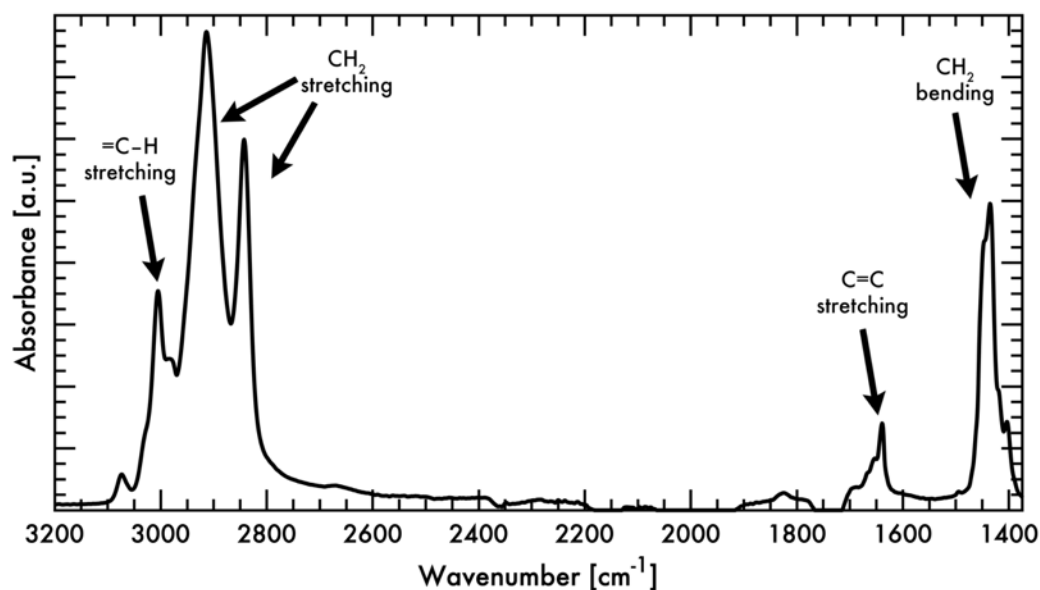


**Figure S2.** Precursor polybutadiene ATR-IR spectrum.

Differential scanning calorimetry (DSC) on the precursor PB was performed using a TA Instruments DSC Q2000. 4 – 5 mg of sample were placed inside an aluminum pan with a standard lid. Under a nitrogen gas flow of 50 mL/min, precursor PB samples were first cooled from 0 to – 80 °C, heated to 65 °C, cooled to – 80 °C, and finally reheated to 65 °C. All heating and cooling rates had a magnitude of 10 °C/min. All samples were examined by DSC in triplicate. No glass transition feature was observed for the precursor PB, suggesting the glass transition temperature ( $T_g$ ) was outside the range of the instrument.

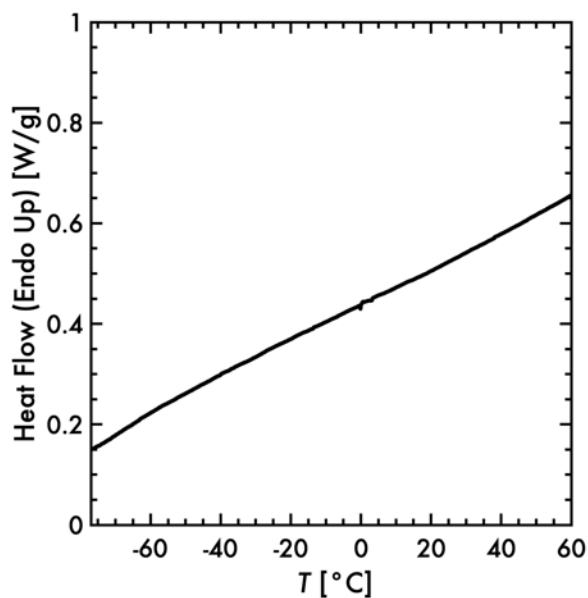


**Figure S3.** Precursor polybutadiene DSC trace.

Small amplitude oscillatory shear (SAOS) on the precursor PB was performed using a TA Instruments ARES-G2 rheometer equipped with 25 mm stainless steel parallel plate geometry and an air cooling system. To achieve sub-ambient temperatures, the plate geometry was enclosed in a convection oven. The polymer was loaded directly onto the lower plate, which was pre-heated to 45 °C. The upper plate was slowly lowered onto the sample to form a plate gap of  $\approx 1$  mm. The sample was then annealed for 30 min, and SAOS was subsequently performed. The sample was then cooled by an increment of 15 °C at a rate of 1 °C/min. This process was repeated for temperatures of 30, 15, 0, and  $-15$  °C. Time-temperature superposition of the precursor PB SAOS data was performed by horizontally shifting the data. The shift factors were fit to an Arrhenius model to extract an activation energy  $E_a^{SAOS}$ .

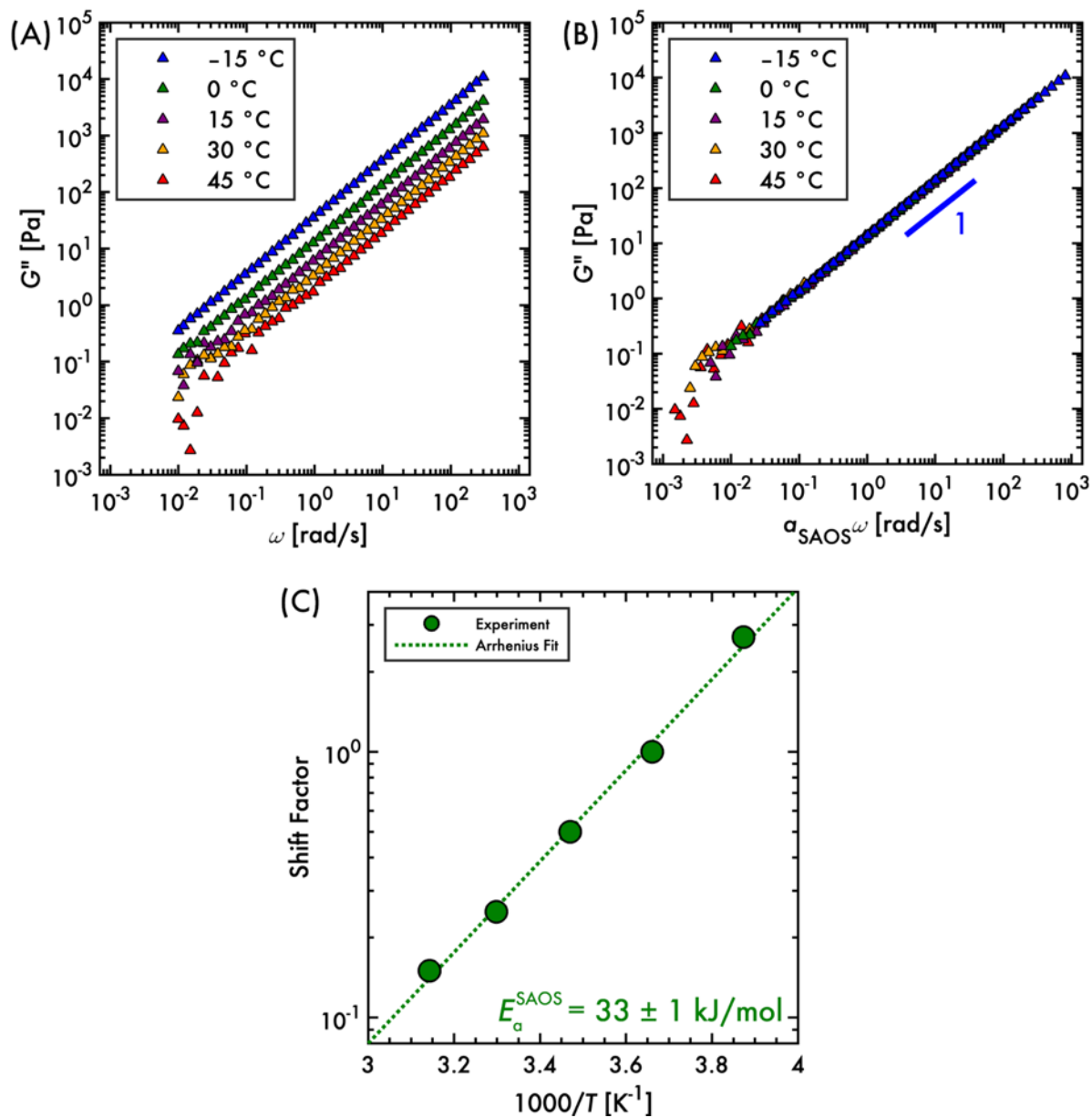


**Figure S4.** Precursor polybutadiene viscous modulus  $G''$  (A) as measured and (B)  $a_{\text{SAOS}}$  shift factors applied. (C) Arrhenius fit of  $a_{\text{SAOS}}$  for precursor PB. For (B) and (C),  $T_R = 0^\circ\text{C}$ .

# <sup>1</sup>H and <sup>13</sup>C nuclear magnetic resonance spectroscopy of dioxaborolane cross-linker

<sup>1</sup>H and <sup>13</sup>C NMR spectroscopy were conducted using a Bruker Advance III 600 MHz NMR spectrometer.

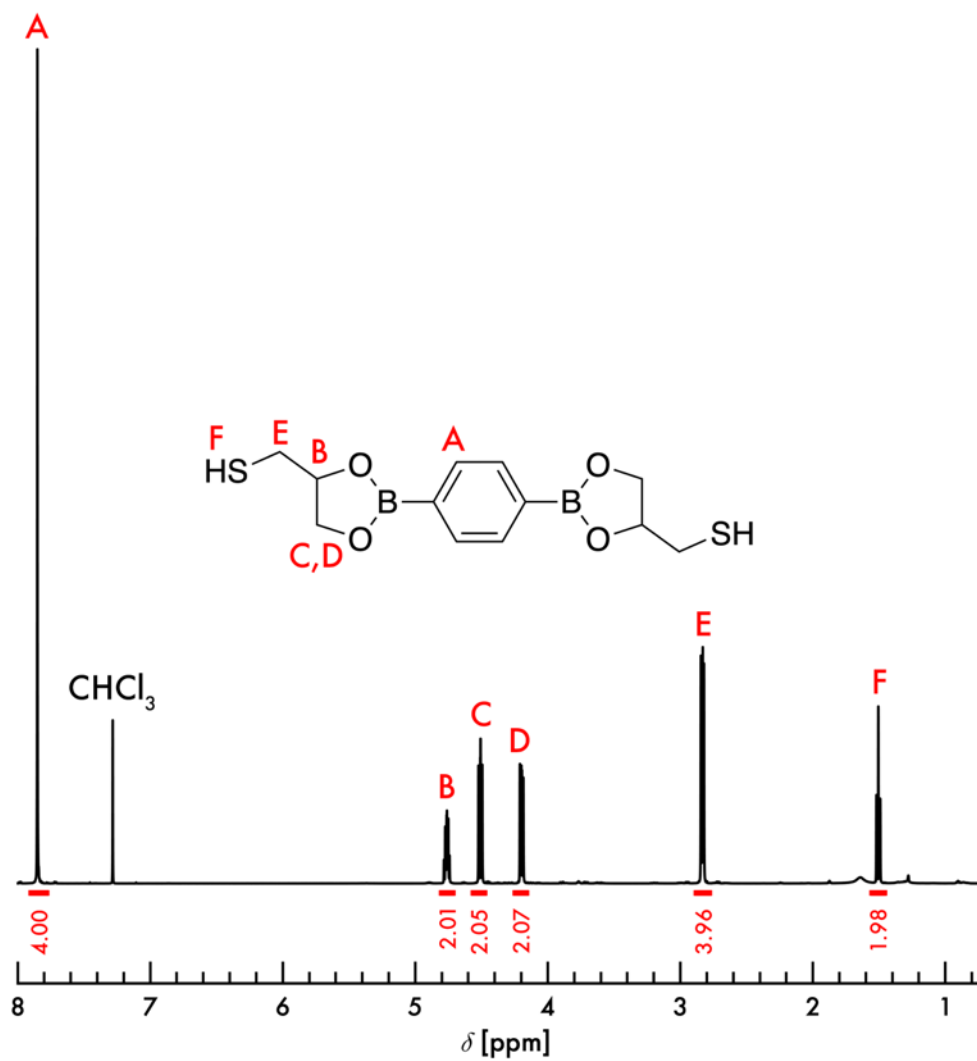


**Figure S5.** <sup>1</sup>H NMR spectrum of dioxaborolane cross-linker in CDCl<sub>3</sub>.

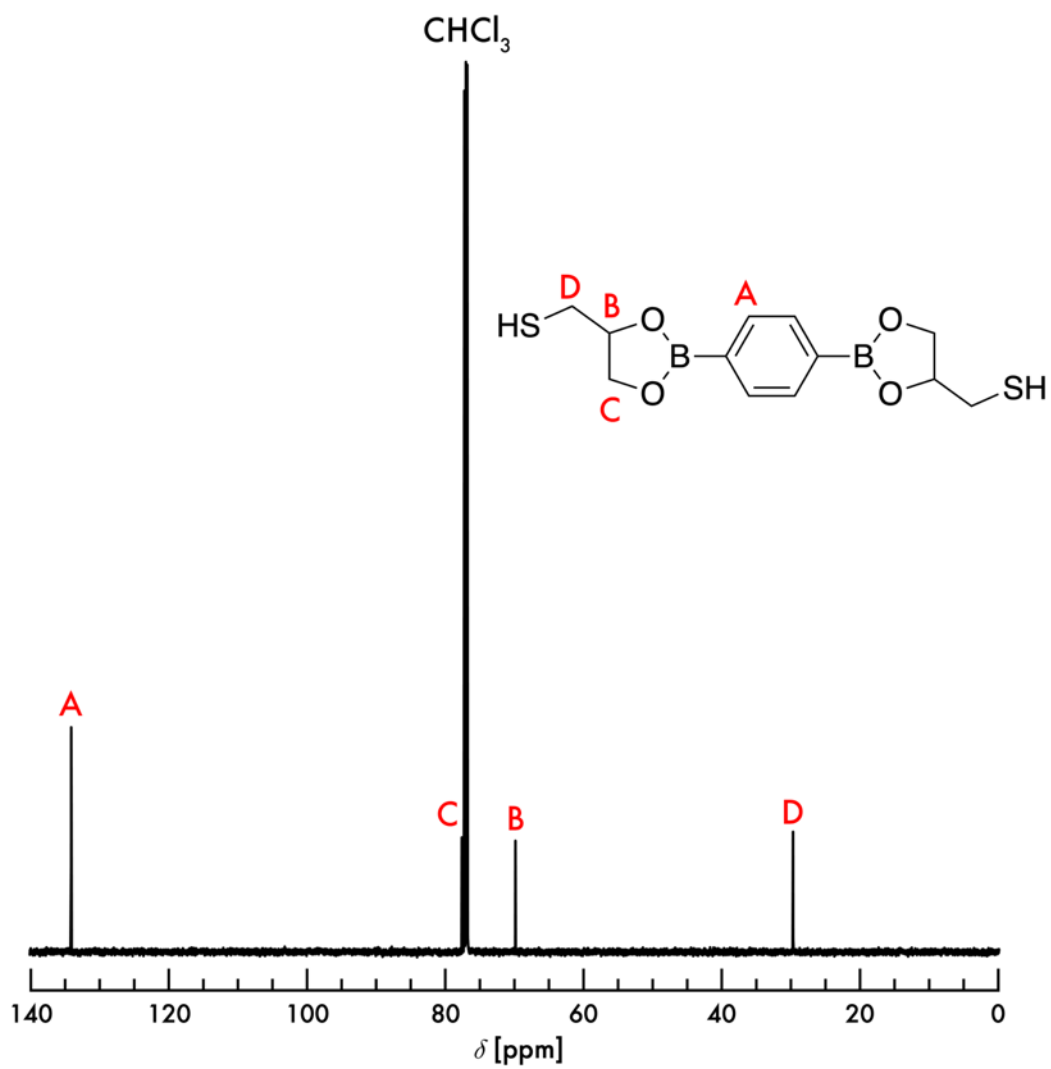


**Figure S6.**  $^{13}\text{C}$  NMR spectrum of dioxaborolane cross-linker in  $\text{CDCl}_3$ .

### PB vitrimer attenuated total reflectance infrared spectroscopy

PB vitrimer ATR-IR spectra were collected using a Nicolet iS50 Fourier Transform Infrared Spectrometer equipped with a Smart iTR Attenuated Total Reflectance Sampling Accessory. The PB backbone displays signals at 1440 (CH<sub>2</sub> bending), 1650 (C=C stretching), 2849 and 2917 (CH<sub>2</sub> stretching), and 3050 cm<sup>-1</sup> (=C-H stretching).<sup>S1</sup> Dioxaborolane cross-linker displays signals at 1478, 1518, and 1600 cm<sup>-1</sup> (aromatic C=C stretching). Benzyl mercaptan displays signals at 1495 and 1600 cm<sup>-1</sup> (aromatic C=C stretching).<sup>S2</sup>

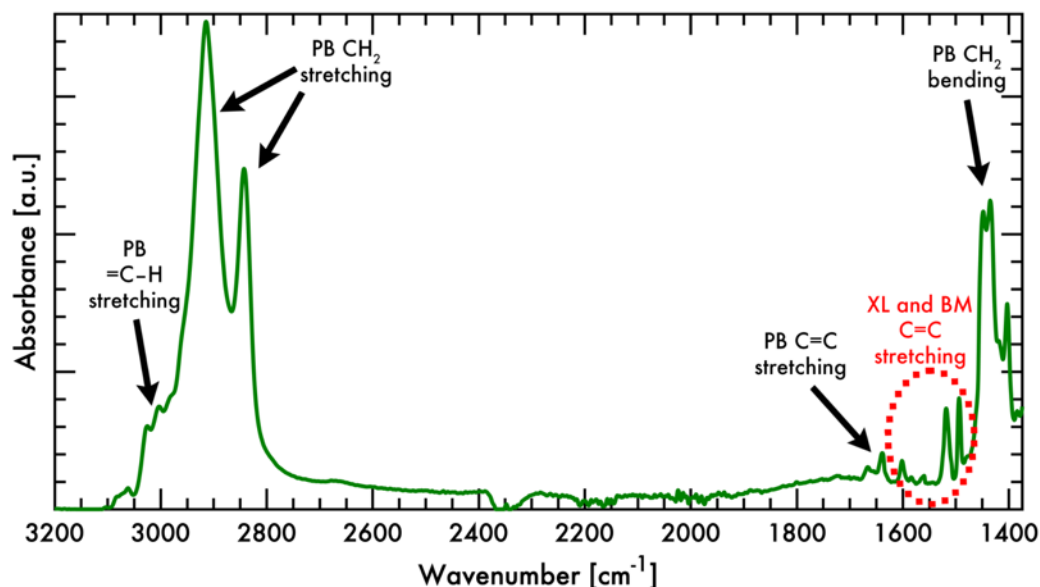


Figure S7. PB- $\nu$ -4 ATR-IR spectrum.

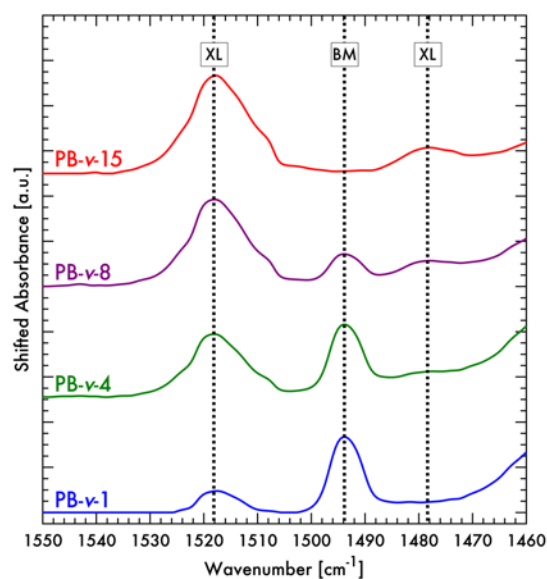


Figure S8. ATR-IR spectra of dioxaborolane cross-link (XL) and benzyl mercaptan (BM) aromatic C=C stretching region for PB vitrimers.

### PB vitrimer thermal characterization

Thermal gravimetric analysis was performed using a TA Instruments TGA Q50. 7 – 8 mg of sample were placed inside an aluminum pan. Under a nitrogen gas flow of 60 mL/min, samples were heated from 25 to 595 °C at a heating rate of 10 °C/min.

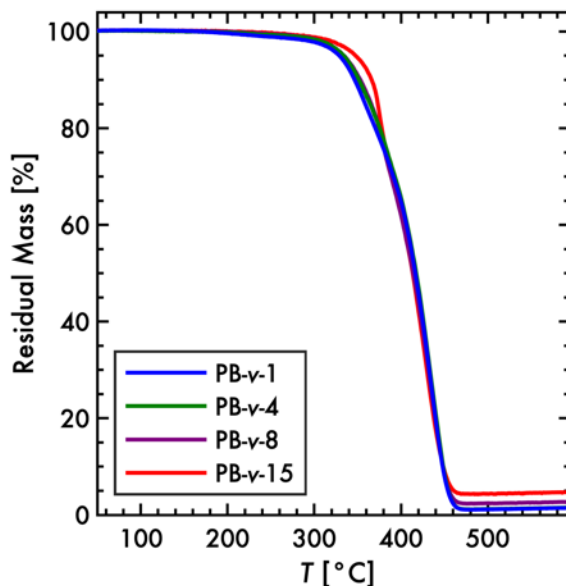


Figure S9. TGA traces for PB vitrimers.

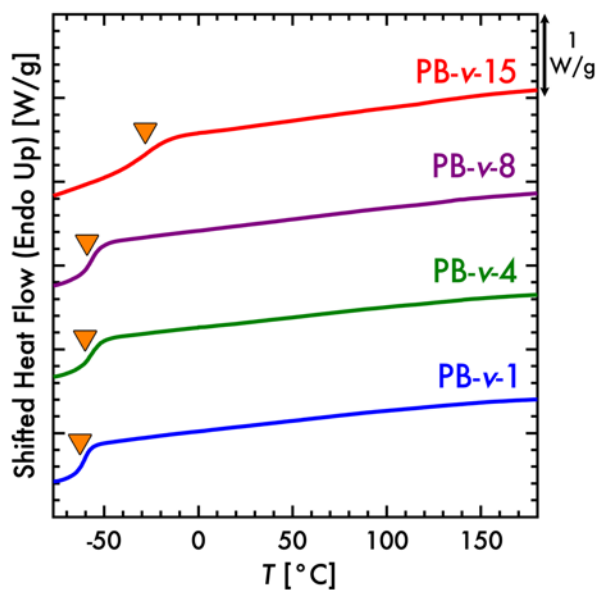


Figure S10. DSC traces for PB vitrimers. Orange triangle marks the glass transition temperature.

### PB vitrimer small-angle X-ray scattering

PB vitrimer samples for small-angle X-ray scattering (SAXS) measurements were prepared using aluminum washers (outer diameter 10 mm, inner diameter 5.3 mm, and thickness 1 mm). 50 mg of PB vitrimer sample were placed inside the washer opening and compression molded at 120 °C. Excess sample was removed using a razor blade.

Lab-scale SAXS was conducted at room temperature using a Bruker Nanostar diffractometer with an Incoatec microfocus X-ray source ( $\lambda = 1.5418 \text{ \AA}$ ). 2D SAXS patterns were collected by a HiStar 2D Multiwire SAXS detector. The data were azimuthally integrated to produce one-dimensional intensity vs. scattering vector ( $I$  vs.  $q$ ) plots using the Bruker SAXS software. Synchrotron-sourced SAXS was conducted at room temperature at DND-CAT beamline 5-ID-D at the Advanced Photon Source in Argonne National Laboratory (Argonne,  $\lambda = 0.7293 \text{ \AA}$ , IL;  $q$ -range:  $0.02\text{--}1.8 \text{ nm}^{-1}$ ). 2D SAXS patterns were collected by a Rayonix MX170-HS detector with a  $3840 \times 3840$  resolution of  $86.6 \times 86.6 \text{ \mu m}$  pixels over an area of  $170 \times 170 \text{ mm}^2$ . The data were azimuthally integrated to produce one-dimensional  $I$  vs.  $q$  plots using custom-made software at the beamline.

Figure S11 features both lab-scale and synchrotron sourced scattering patterns for PB vitrimers. The upturn at low  $q$  represents background scattering, while the plateau at high  $q$  depicts incoherent scattering.

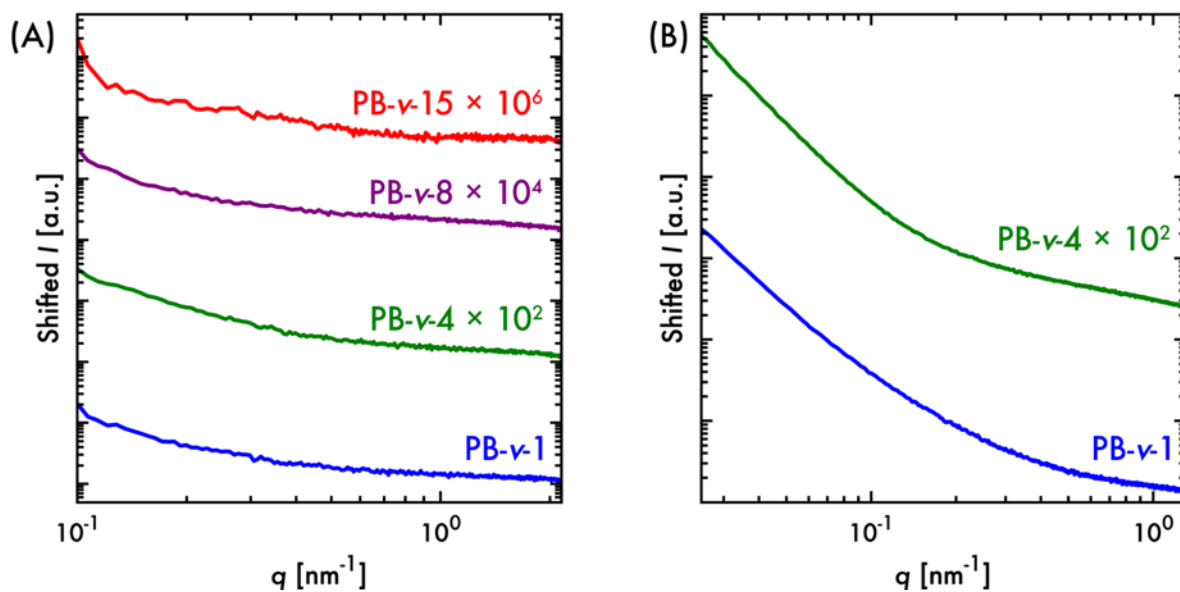


**Figure S11.** Small angle X-ray scattering patterns. (A) Lab-scale and (B) synchrotron-sourced.

### Estimated insoluble fraction for networks with a statistical cross-link distribution

To estimate the expected insoluble fraction possible for PB vitrimers, a statistical model was used.<sup>3</sup> In this model, which assumes that the dioxaborolane cross-linker adds to the PB backbone in a statistical manner,  $N$  is the degree of polymerization of the backbone chain and  $N_S$  is the number of cross-links on the backbone. The number fraction of chains with  $N$  segments and  $N_S$  cross-links is described as the product of two separate distributions

$$\phi(N, N_S) = \theta(N) \times \psi(N, N_S) = \theta(N) \frac{N!}{(N - N_S)! N_S!} p^{N_S} (1 - p)^{N - N_S} \quad (\text{S1})$$

where  $\theta$  is the molar mass distribution of the precursor PB chains (as determined from SEC analysis, see Figure 1A), and  $\psi$  is the  $N_S$  distribution for chains with length  $N$ .  $\psi$  is assumed to follow a binomial distribution, where  $p$  is the targeted mole fraction of cross-link bearing repeat units per backbone chain; *i.e.*,

$$p = N_{XL}/N_n \quad (\text{S2})$$

where  $N_{XL}$  is the targeted number of cross-links per chain and  $N_n$  is the number average molar mass of the precursor PB. Because all chains encompassed by  $\theta(N)$  at a particular  $N$  value have identical degrees of polymerization, the number and weight fractions of chains of PB chains with different  $N_S$  are equivalent.<sup>4</sup> Consequently, the expected insoluble fraction corresponds to

$$\text{insoluble fraction} = \sum_{N=1}^{\infty} \phi(N, N_S \neq 0) = 1 - \sum_{N=1}^{\infty} \phi(N, N_S = 0) \quad (\text{S3})$$

### PB vitrimer strain amplitude sweeps

For strain amplitude sweep measurements, a sample disc was placed onto the lower plate, preheated to either 180 °C or 100 °C. The upper plate and hood were slowly lowered onto the sample to form a gap of  $\approx 1.5$  mm. After a 60 min annealing, small amplitude oscillatory shear measurements were performed at an angular frequency  $\omega = 1$  rad/s. The strain amplitude was increased from 0.01 to 100%.

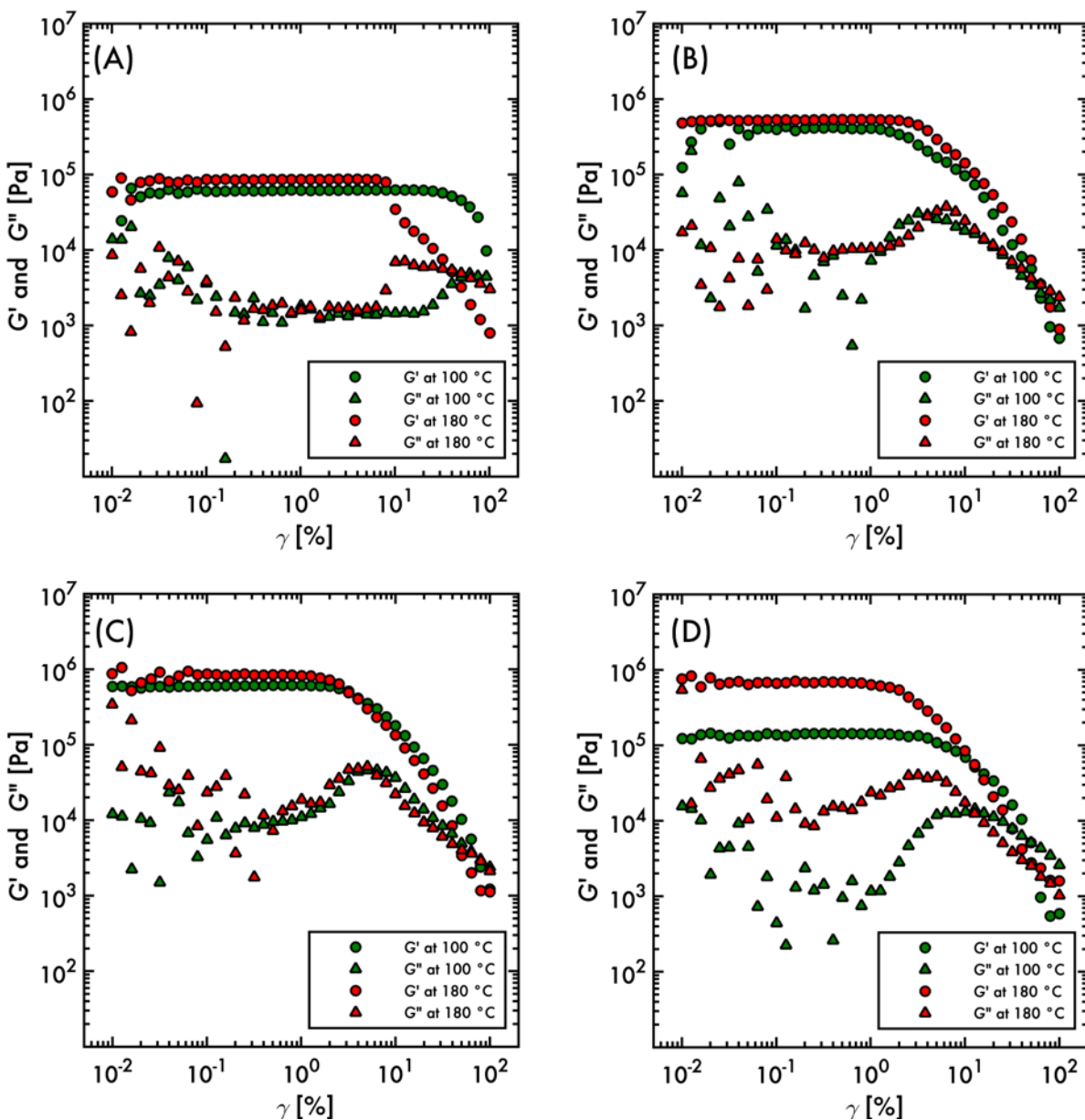


**Figure S12.** Strain amplitude sweeps at  $\omega = 1$  rad/s. (A) PB- $\nu$ -1, (B) PB- $\nu$ -4, (C) PB- $\nu$ -8, and (D) PB- $\nu$ -15.

## Parameters for rheological measurements

**Table S1.** Parameters for rheological measurements

Sample ID	$\gamma_0$ for SAOS and stress relaxation [%]	$\epsilon_0$ for creep [Pa]
PB-v-1	3	900
PB-v-4	1	900
PB-v-8	0.8	1000
PB-v-15	0.4	1100

### Preconditioning procedure for rheological measurements

To improve the reproducibility of SAOS and stress relaxation measurements, the following experiment protocol was used. A sample disc was placed onto the lower plate, preheated to 180 °C. The upper plate and hood were slowly lowered onto the sample to form a gap of  $\approx 1.5$  mm. After a 60 min annealing, a preconditioning stress relaxation cycle was performed. During a single cycle, a step strain with magnitude  $\gamma_0$  was applied for 15 minutes (see Table S1). After 15 minutes the strain was released, and the sample was allowed to anneal in the absence of an applied strain for 15 minutes. A total of 5 preconditioning cycles were performed at 180 °C. Afterwards, the sample was cooled to 160 °C at a rate of 1 °C/min, annealed at 160 °C for 60 min, and exposed to 5 preconditioning cycles. After preconditioning, SAOS was performed. Following the SAOS measurement, 5 more preconditioning stress relaxation cycles were performed. Subsequently, stress relaxation was performed for 8 hrs. The same procedure was repeated for temperatures of 140, 120, 100, and 80 °C. Figure S13 depicts the stress relaxation modulus  $G$  during the preconditioning cycles and final stress relaxation measurement (*i.e.*, Cycle 6) for PB-v-4. For creep compliance and recovery measurements, a similar preconditioning procedure was used.

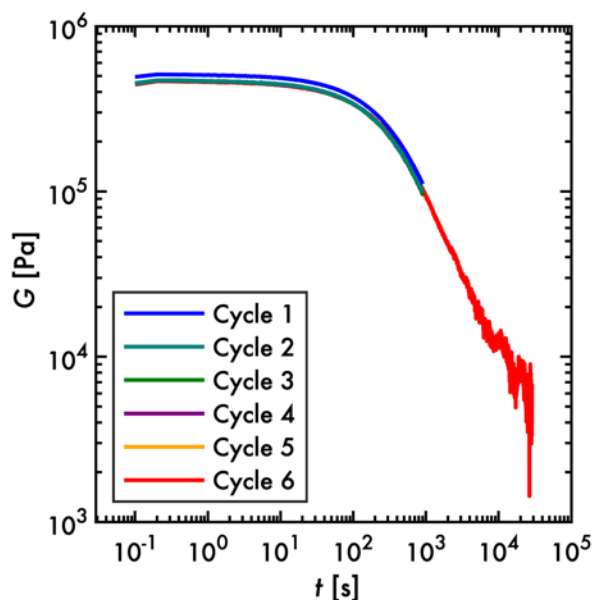


**Figure S13.** Representative pre-conditioning cycle for PB-v-4 at 160 °C. Data for Cycle 6 are the same data presented in Figure 5 in the main manuscript.

SAOS and creep data for PB- $\nu$ -1, PB- $\nu$ -8, and PB- $\nu$ -15

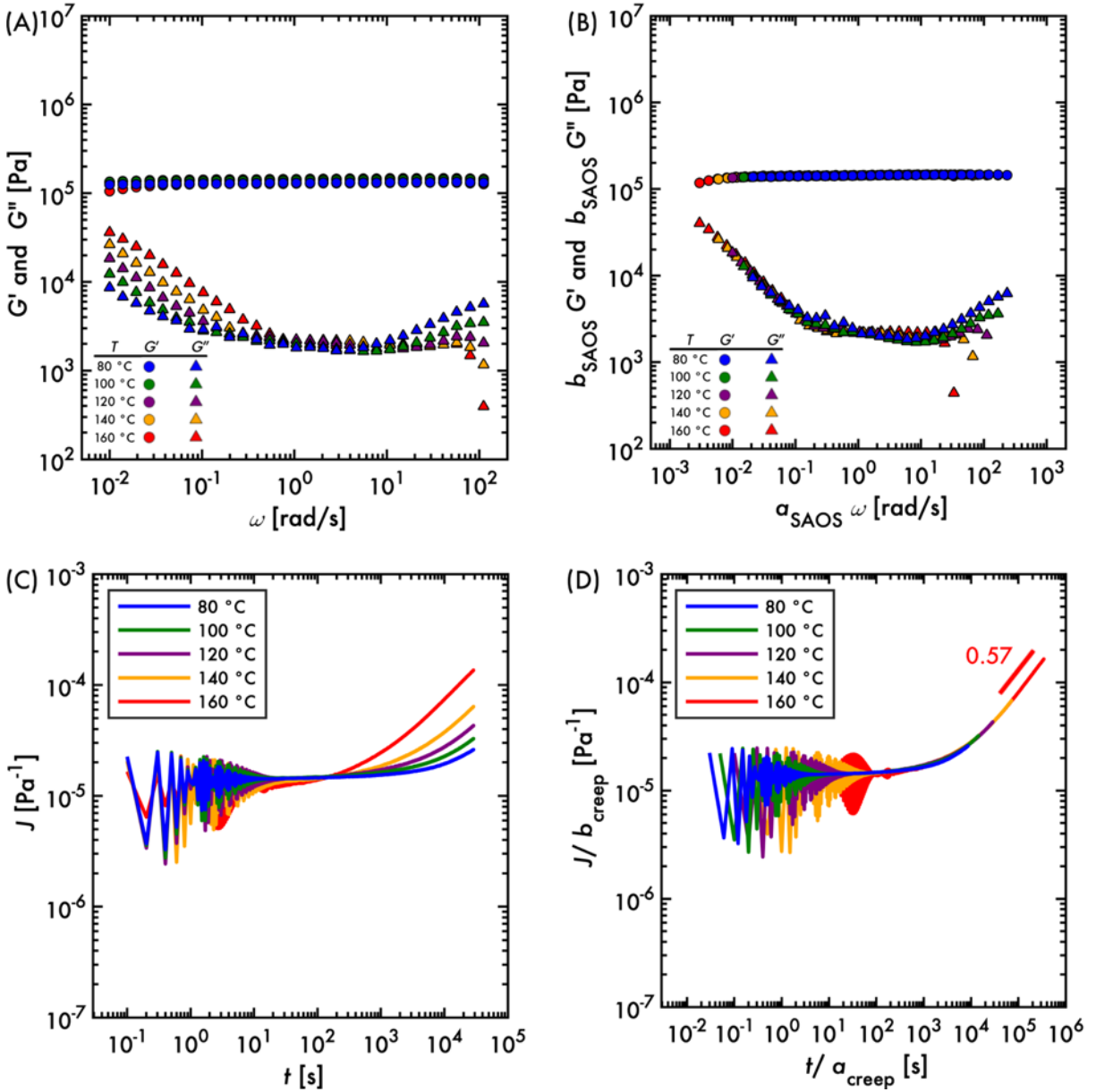


**Figure S14.** Linear viscoelastic measurements of PB- $\nu$ -1. (A) SAOS as measured and (B) with  $a_{SAOS}$  horizontal shift factors applied. (C) Creep as measured and (D) with  $a_{creep}$  horizontal shift factors applied. Reference temperature for both  $a_{SAOS}$  and  $a_{creep}$  is 120 °C.

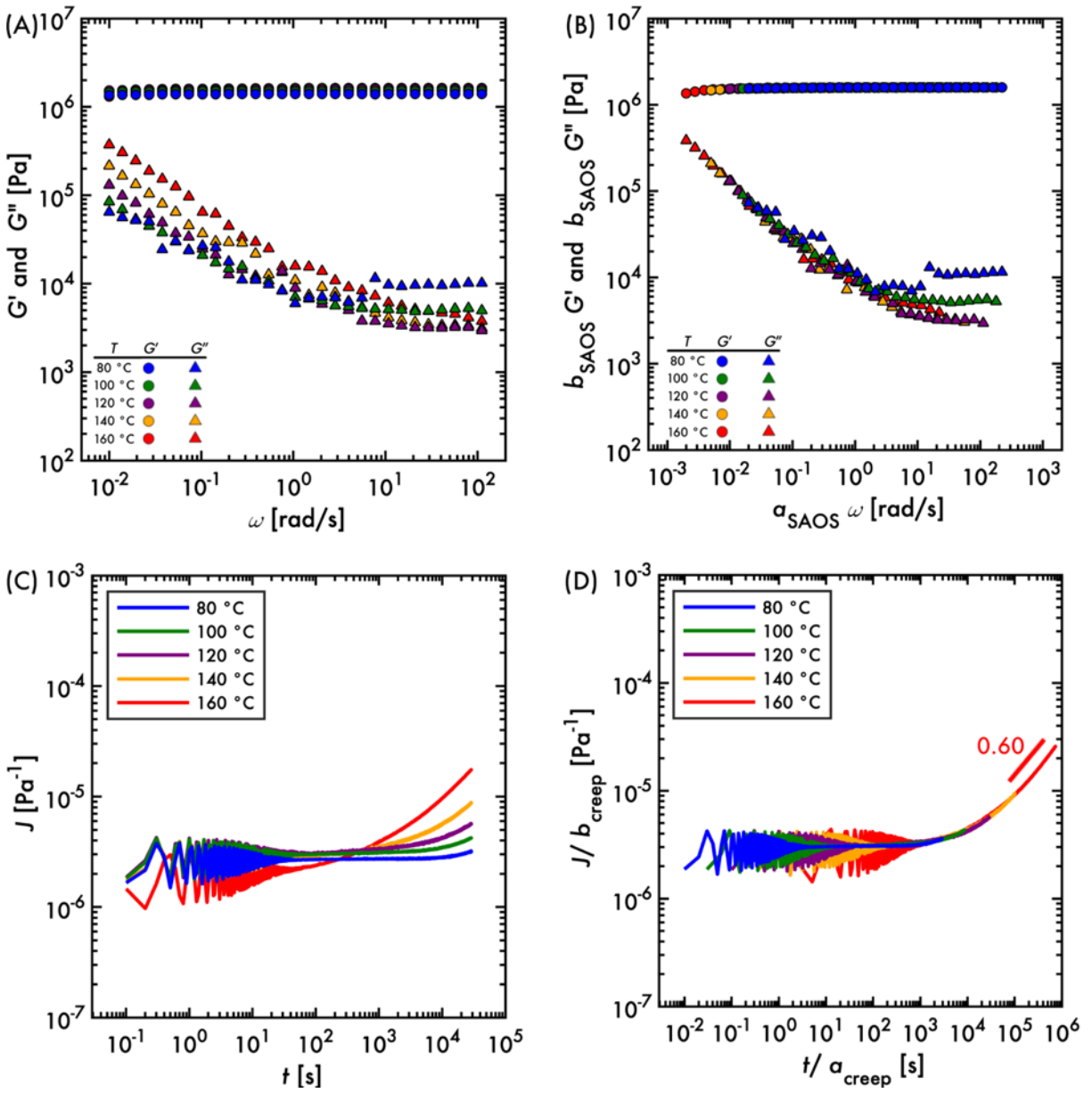


**Figure S15.** Linear viscoelastic measurements of PB-v-8. (A) SAOS as measured and (B) with  $a_{SAOS}$  horizontal shift factors applied. (C) Creep as measured and (D) with  $a_{creep}$  horizontal shift factors applied. Reference temperature for both  $a_{SAOS}$  and  $a_{creep}$  is 120 °C.

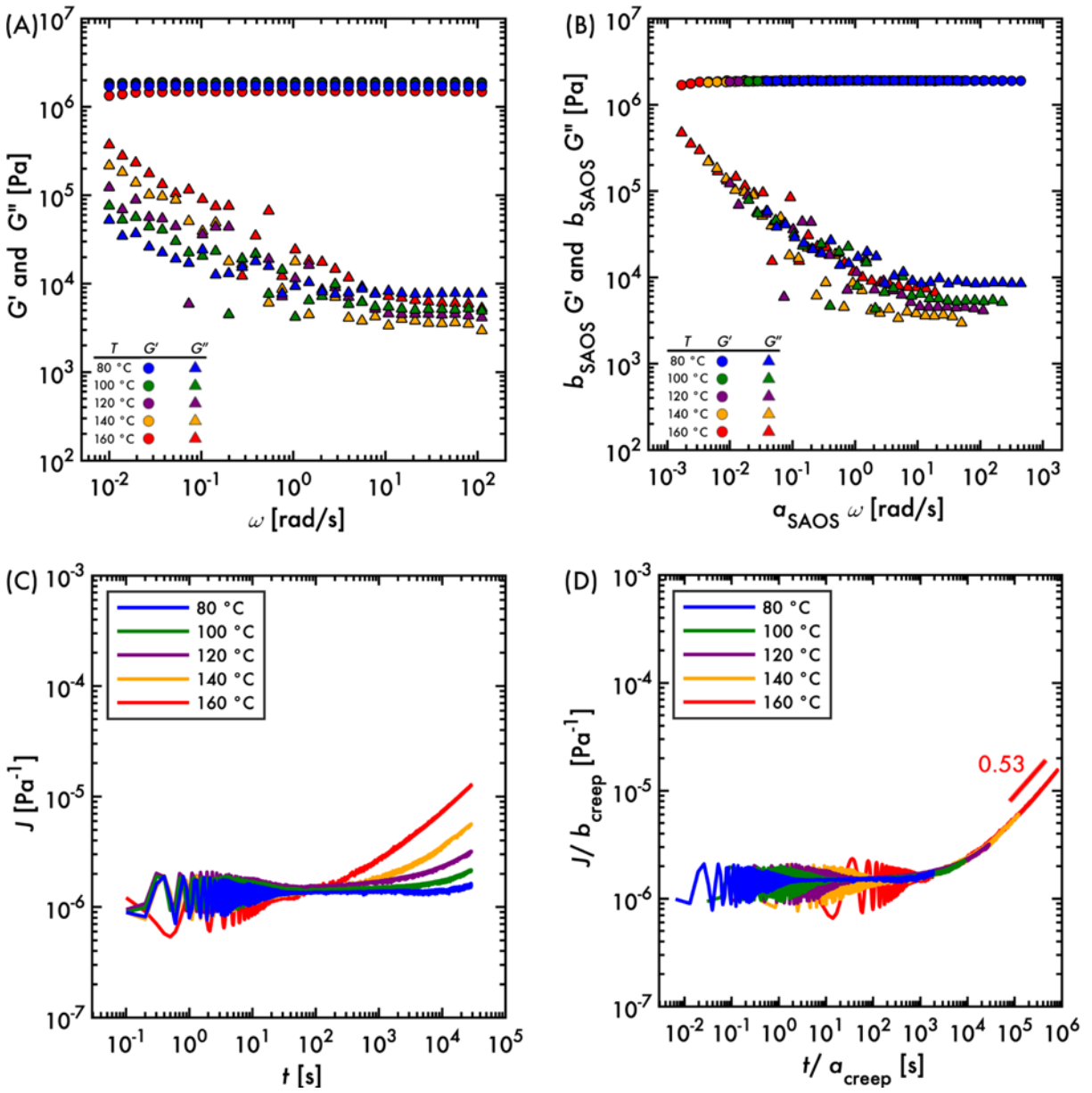


**Figure S16.** Linear viscoelastic measurements of PB-v-15. (A) SAOS as measured and (B) with  $a_{SAOS}$  horizontal shift factors applied. (C) Creep as measured and (D) with  $a_{creep}$  horizontal shift factors applied. Reference temperature for both  $a_{SAOS}$  and  $a_{creep}$  is 120 °C.

*tan δ* data

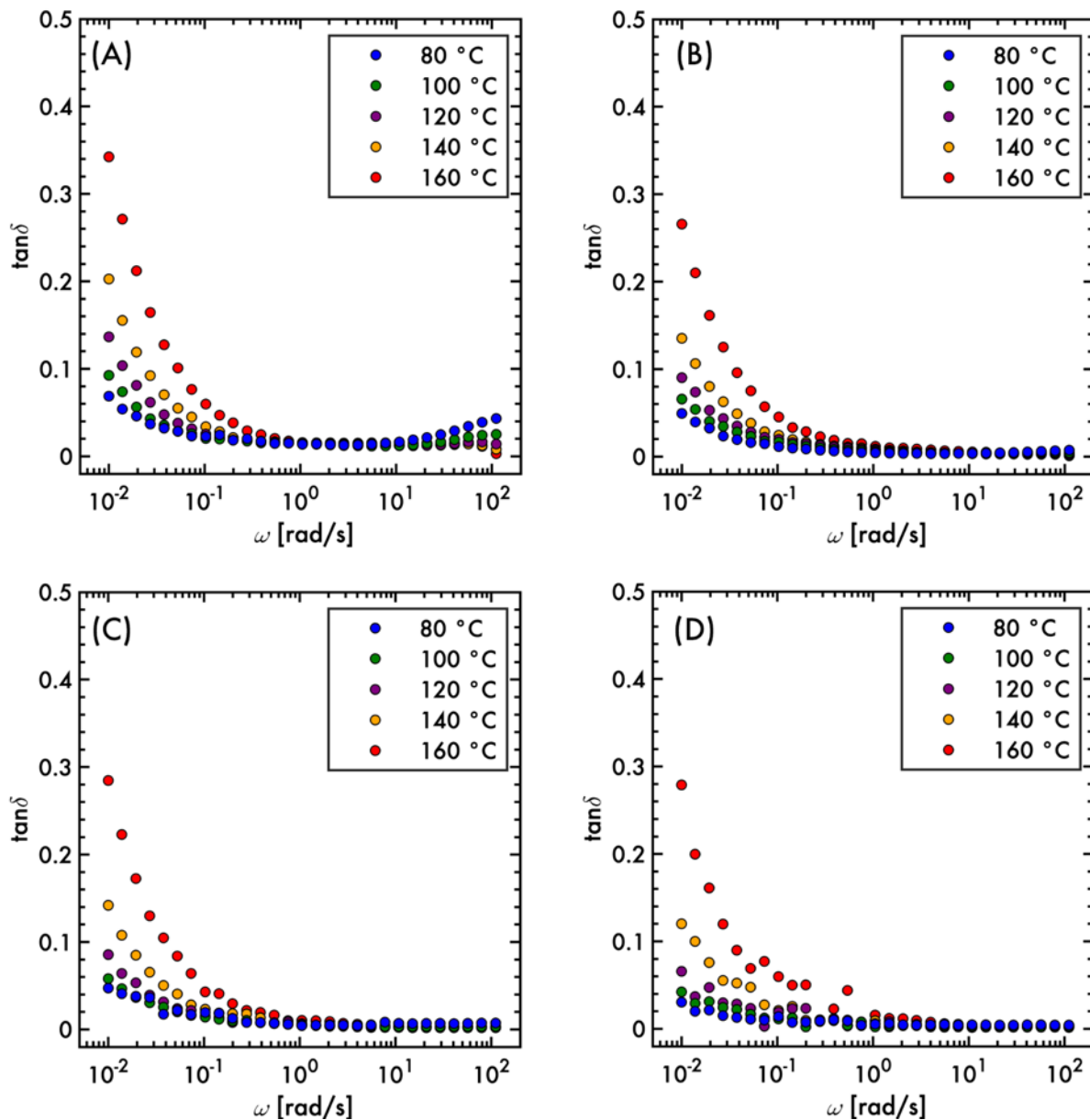


**Figure S17.** Raw  $\tan \delta$  data for (A) PB- $\nu$ -1, (B) PB- $\nu$ -4, (C) PB- $\nu$ -8, and (D) PB- $\nu$ -15.

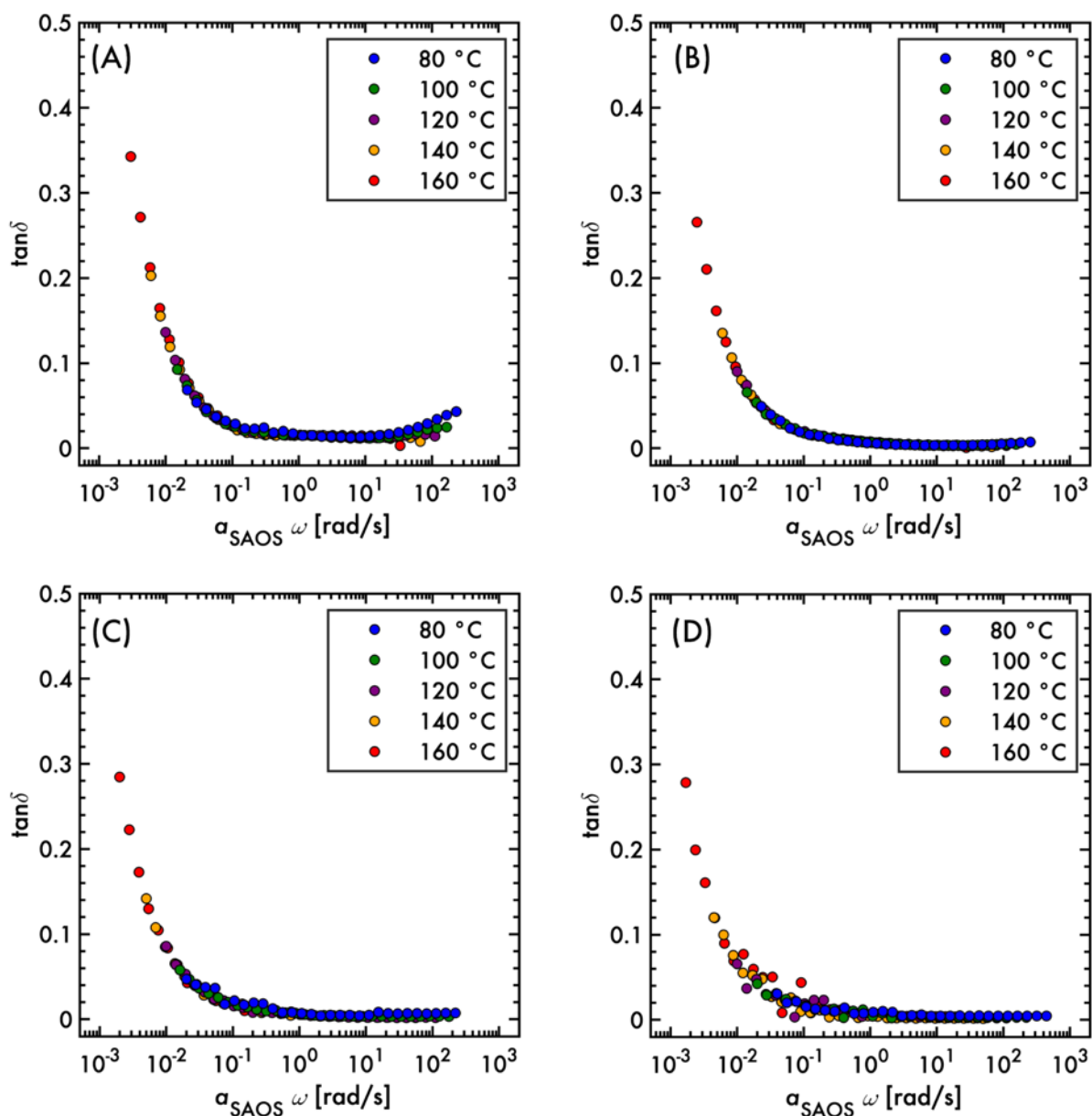


**Figure S18.**  $\tan \delta$  master curves for (A) PB- $\nu$ -1, (B) PB- $\nu$ -4, (C) PB- $\nu$ -8, and (D) PB- $\nu$ -15. For all panels, the reference temperature is 120 °C.

### Creep Recovery Compliance Data

The creep recovery compliance ( $J_{rec}$ ) was determined by

$$J_{rec} = \frac{\gamma_f - \gamma}{\sigma} \quad (S4)$$

where  $\gamma$  is the strain,  $\sigma$  is the applied stress during creep, and  $\gamma_f$  is the value of the strain when  $\sigma$  was removed.

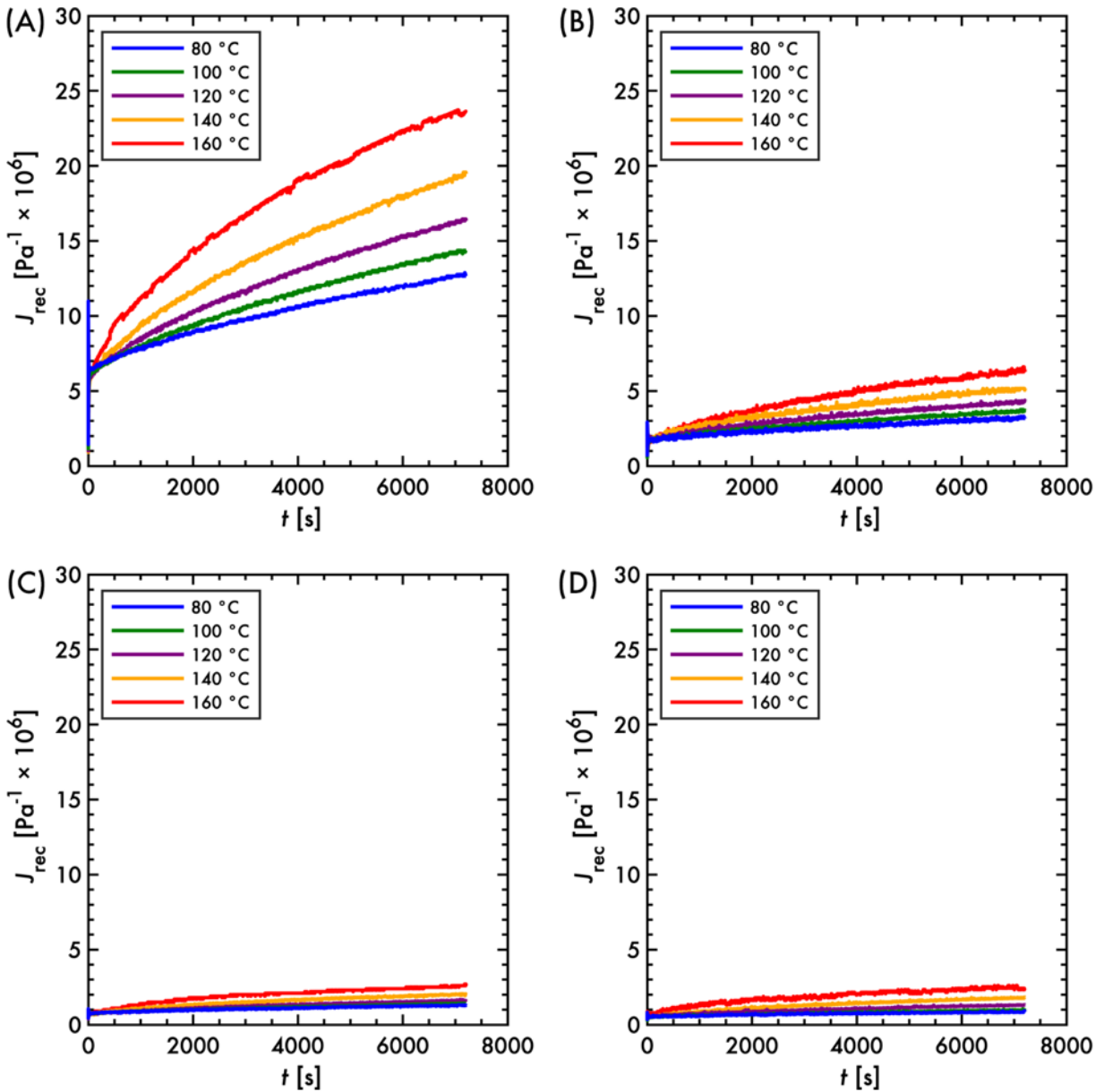


**Figure S19.** Creep recovery compliance ( $J_{rec}$ ) for (A) PB- $\nu$ -1, (B) PB- $\nu$ -4, (C) PB- $\nu$ -8, and (D) PB- $\nu$ -15.

$a_{SAOS}$  and  $a_{creep}$  shift factors for PB- $\nu$ -1, PB- $\nu$ -8, and PB- $\nu$ -15

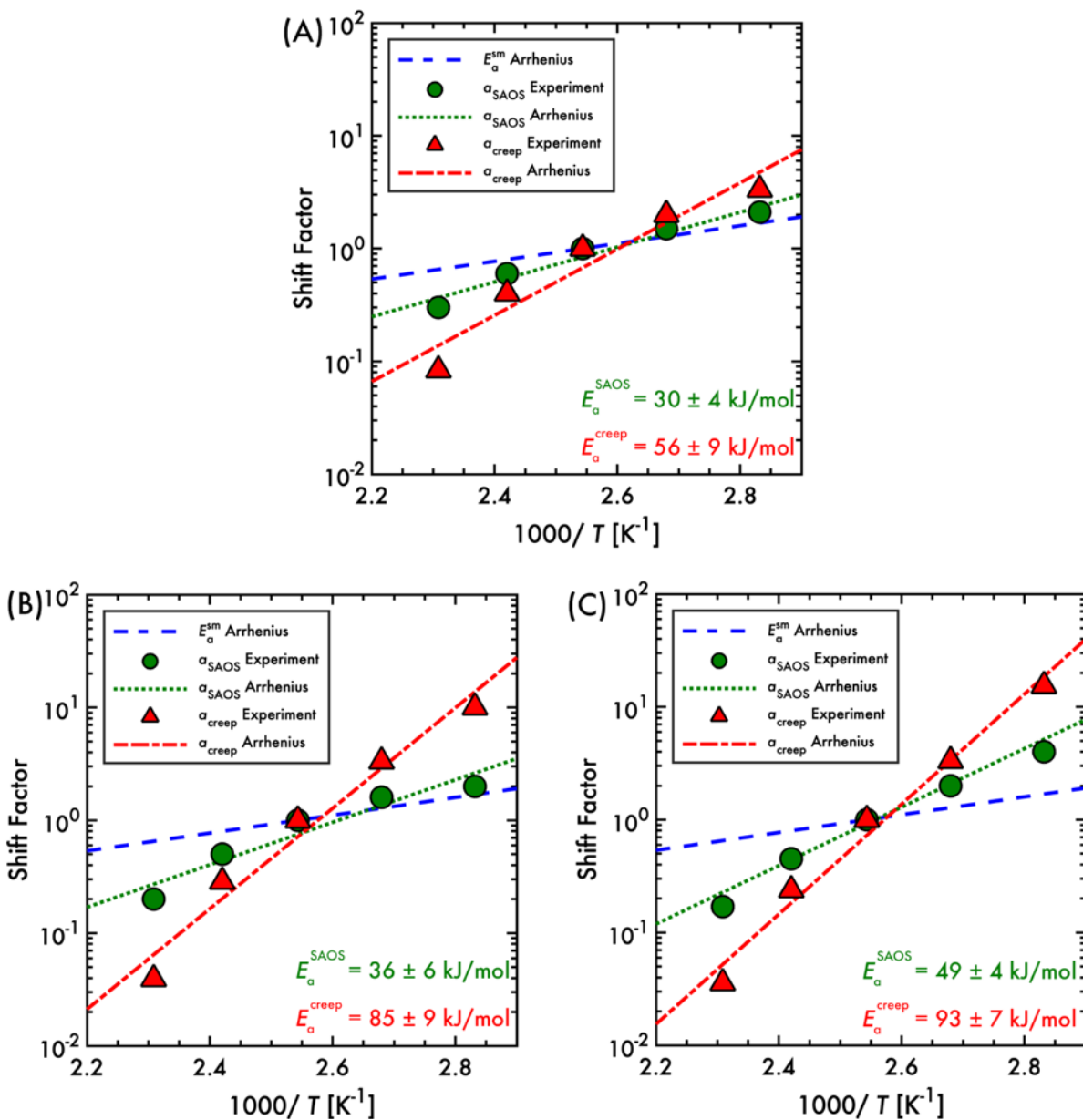


**Figure S20.**  $a_{SAOS}$  and  $a_{creep}$  data and Arrhenius fits for (A) PB- $\nu$ -1, (B) PB- $\nu$ -8, and (C) PB- $\nu$ -15. For all panels, the reference temperature is 393.15 K.

## Plateau moduli and vertical shift factors

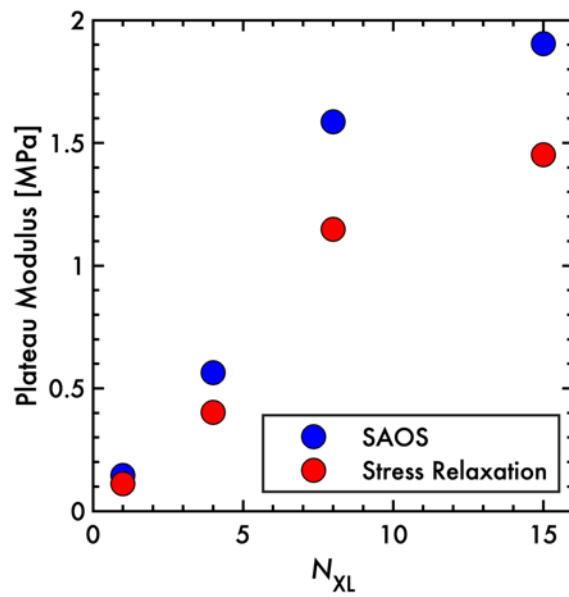


**Figure S21.** SAOS and stress relaxation plateau moduli at 120 °C vs.  $N_{XL}$ .

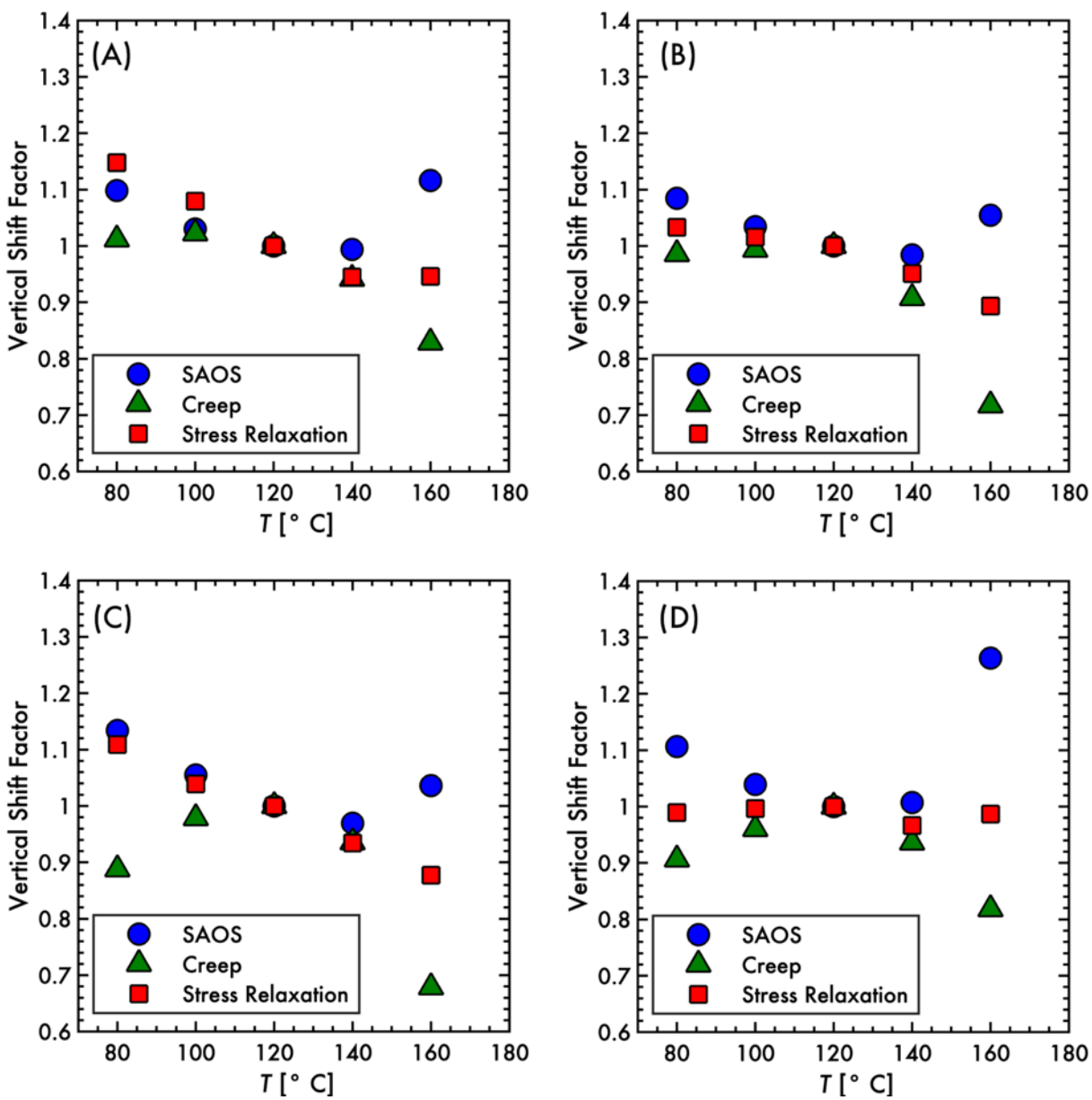


**Figure S22.** SAOS, creep, and stress relaxation vertical shift factors for (A) PB- $\nu$ -1, (B) PB- $\nu$ -4, and (C) PB- $\nu$ -8, and (D) PB- $\nu$ -15. For all panels, the reference temperature is 120 °C.

Stress relaxation for PB- $\nu$ -1, PB- $\nu$ -8, and PB- $\nu$ -15

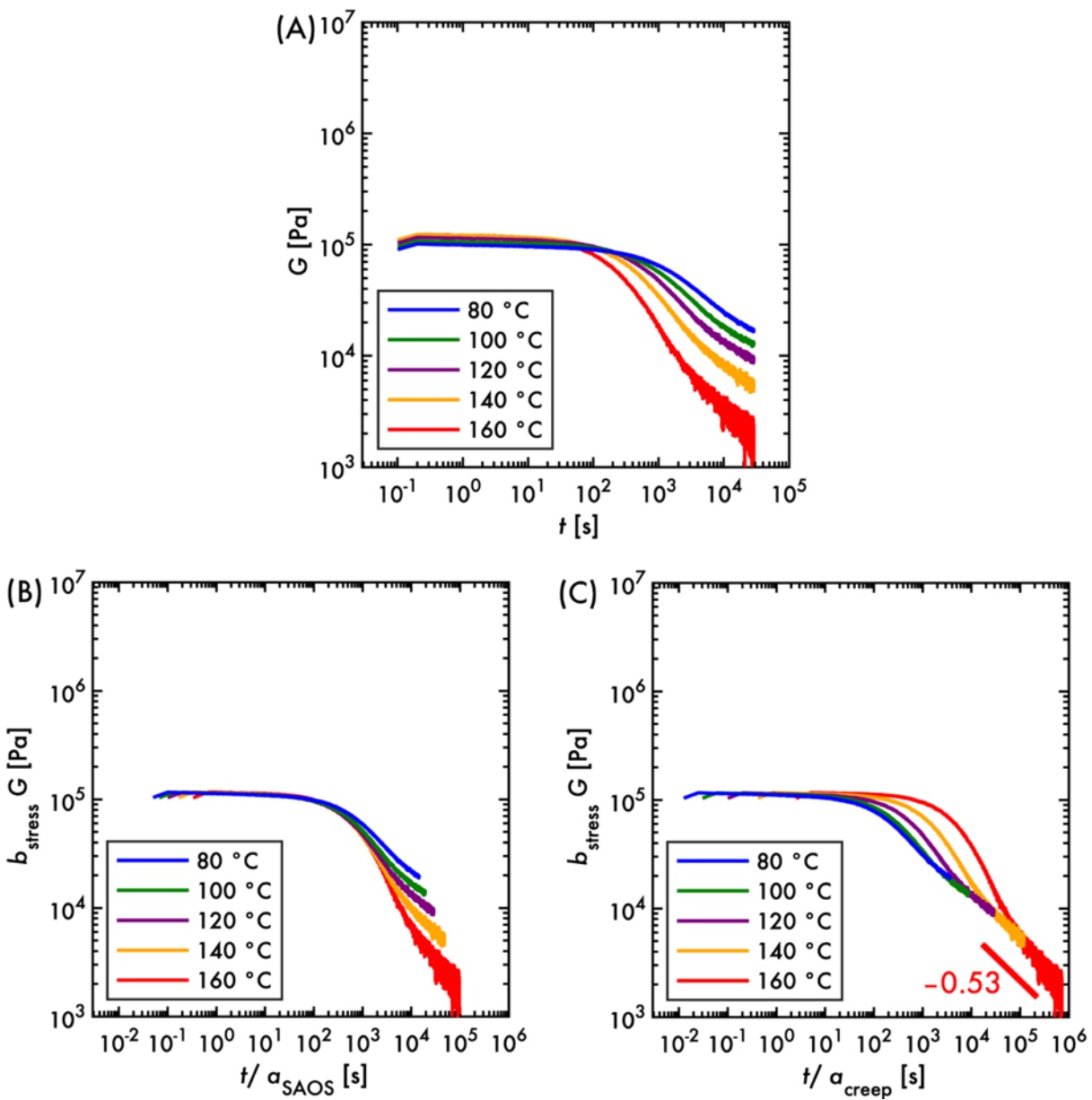


**Figure S23.** Stress relaxation of PB- $\nu$ -1 (A) as measured, (B) with  $a_{\text{SAOS}}$ , and (C)  $a_{\text{creep}}$  horizontal shift factors applied. Reference temperature for both  $a_{\text{SAOS}}$  and  $a_{\text{creep}}$  is 120 °C.

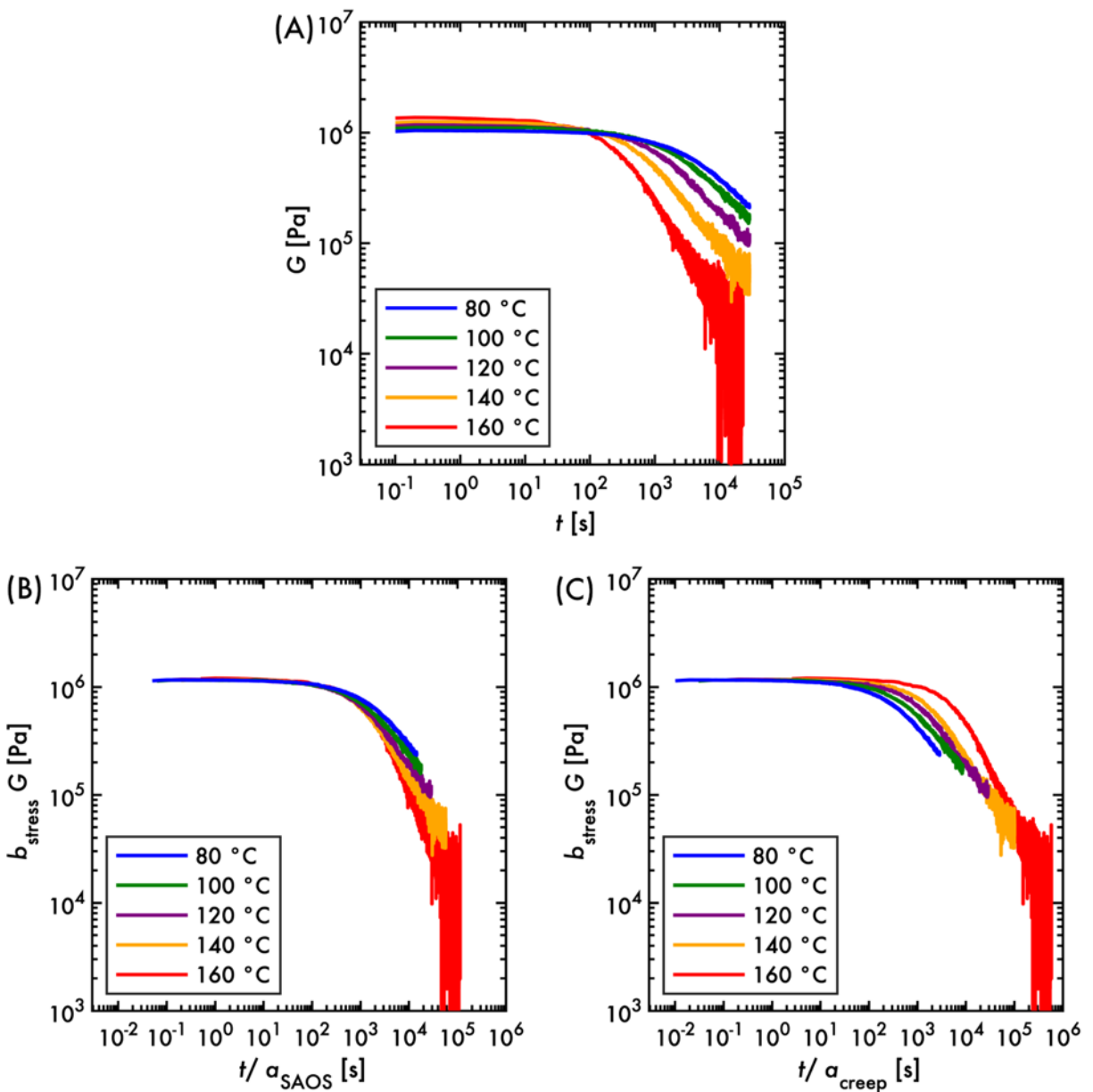


**Figure S24.** Stress relaxation of PB-v-8 (A) as measured, (B) with  $a_{\text{SAOS}}$ , and (C)  $a_{\text{creep}}$  horizontal shift factors applied. Reference temperature for both  $a_{\text{SAOS}}$  and  $a_{\text{creep}}$  is 120 °C.

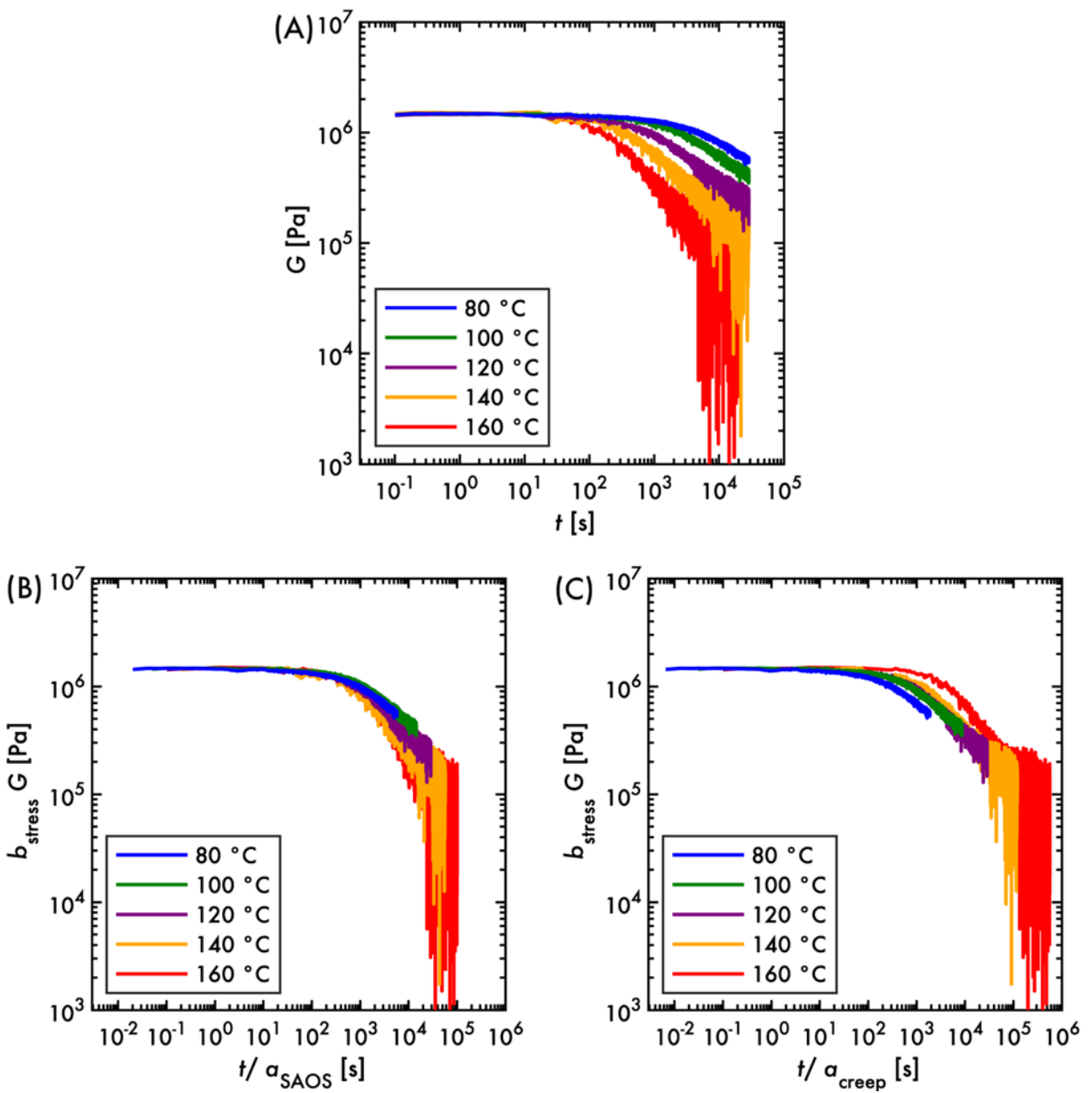


**Figure S25.** Stress relaxation of PB- $\nu$ -15 (A) as measured, (B) with  $a_{SAOS}$ , and (C)  $a_{creep}$  horizontal shift factors applied. Reference temperature for both  $a_{SAOS}$  and  $a_{creep}$  is 120 °C.

## 24 hr creep of PB- $\nu$ -15

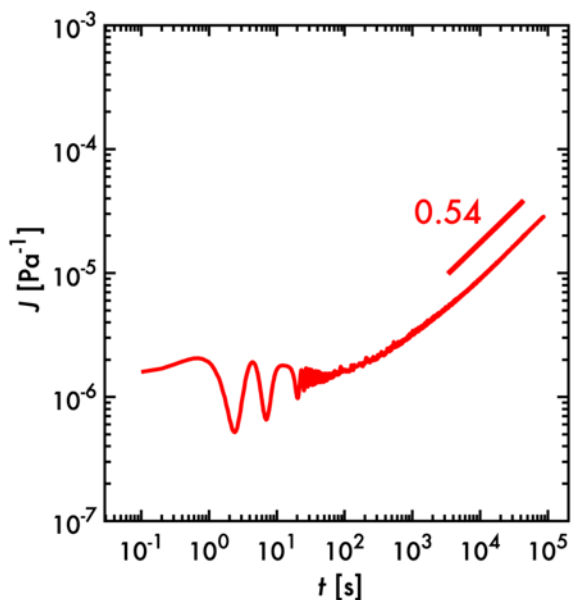
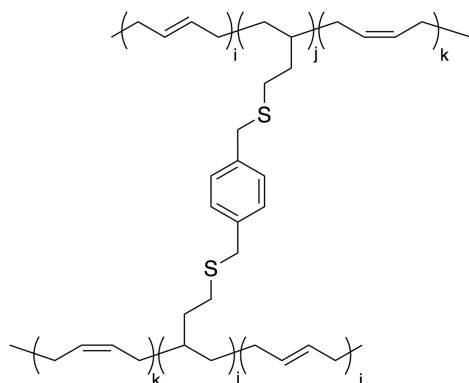


Figure S26. 24 hr creep for PB- $\nu$ -15 at 160 °C.

### Static cross-link PB thermoset synthesis and SAOS, creep, and stress relaxation

Scheme S1 depicts the chemical structure of the static cross-link PB thermoset control sample. To prepare the PB thermoset with static cross-links, polybutadiene (2.00 g, 4.4 mmol of vinyl groups), 1,4-benzenedimethanethiol (0.378 g, 2.2 mmol), 2,2-dimethoxy-2-phenylacetophenone (0.1128 g, 0.44 mmol), and dry chloroform (9.6 mL) were mixed in a scintillation vial, transferred into a 50 mL roundbottom single neck Schlenk flask, and degassed through three freeze-pump-thaw cycles. Cross-linking was performed by exposing the reaction mixture to UV light (MelodySusie Model DR-301Z,  $\lambda = 365$  nm, Flux =  $800 \mu\text{W}/\text{cm}^2$ ) for 1 hr. After UV exposure, the resulting gel was doped with 0.1 mL of a solution containing 0.002 g of Irganox 1520 dissolved in dry chloroform, and then stored in the dark at ambient temperature for 24 hrs. The gel was then transferred to a scintillation vial and dried under reduced pressure at 75 °C for 18 hrs to yield 1.70 g of a yellow-green solid.

Scheme S1. Static cross-link PB thermoset chemical structure.



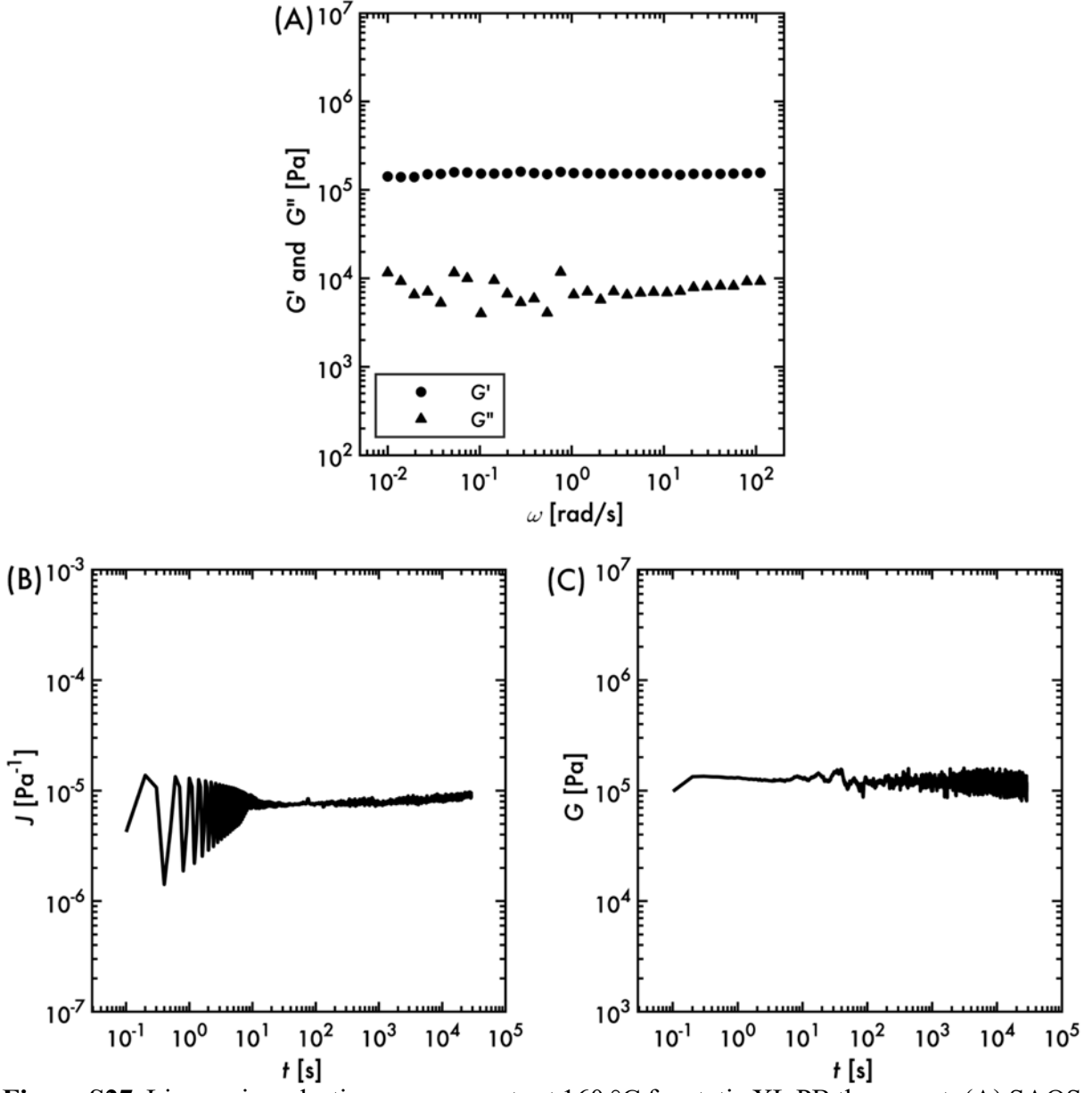


**Figure S27.** Linear viscoelastic measurements at 160 °C for static XL PB thermoset: (A) SAOS, (B) creep, and (C) stress relaxation.

### Prony series analysis for PB- $\nu$ -4

The frequency range of SAOS data can be extended using a Prony series analysis. In this empirical method, a series of Maxwell exponential decays are fit to stress relaxation data collected at the same temperature as the SAOS measurement

$$G = \sum_{i=1}^n G_i \exp\left(\frac{-t}{\tau_i}\right) \quad (\text{S5})$$

where  $t$  is time, and  $G_i$  and  $\tau_i$  are the plateau modulus and relaxation time, respectively, of the  $i$ th mode. The elastic and viscous moduli ( $G'$  and  $G''$ ) are then estimated by

$$G' = \sum_{i=1}^n \frac{G_i \tau_i^2 \omega^2}{(1 + \tau_i^2 \omega^2)} \quad (\text{S6})$$

$$G'' = \sum_{i=1}^n \frac{G_i \tau_i \omega}{(1 + \tau_i^2 \omega^2)} \quad (\text{S7})$$

where  $\omega$  is the angular frequency.<sup>S5,S6,S7</sup>

Figure S28A is the stress relaxation modulus of PB- $\nu$ -4 at 160 °C fit to a Prony series with 3 modes. The six fitting parameters are listed in Table S2. Figure S28B compares the estimated  $G'$  and  $G''$  to the measured SAOS data. The Prony series analysis estimates a  $G'$ - $G''$  crossover to occur at  $\omega_{cross}(160\text{ }^\circ\text{C}) = 0.0012$  rad/s. The dioxaborolane cross-link lifetime at 120 °C ( $\tau_{XL}$ ) is then calculated by

$$\tau_{XL} = \frac{1}{a_{SAOS}(160\text{ }^\circ\text{C})\omega_{cross}(160\text{ }^\circ\text{C})} = 4000\text{ s} \quad (\text{S8})$$

where  $a_{SAOS}(160\text{ }^\circ\text{C})$  is the 160 °C horizontal shift factor estimated from the SAOS data.

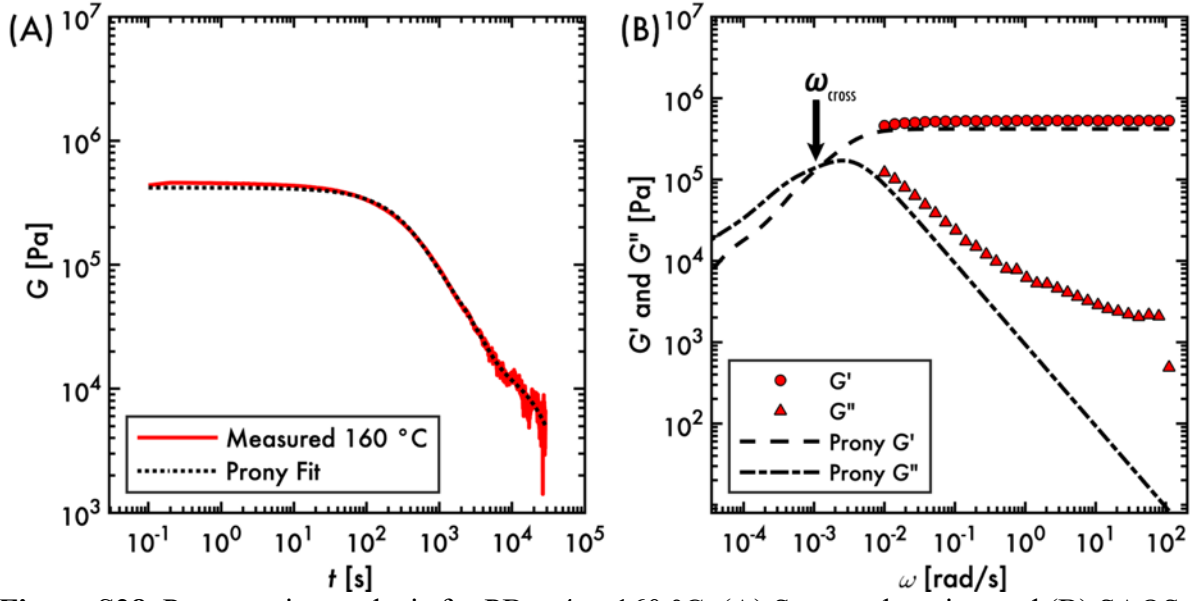


**Figure S28.** Prony series analysis for PB- $\gamma$ -4 at 160 °C. (A) Stress relaxation and (B) SAOS.

**Table S2.** Prony series fitting parameters for PB- $\gamma$ -4 at 160 °C.

$i$	$G_i$ [Pa]	$\tau_i$ [s]
1	300000	340
2	103000	1700
3	18000	23000

### Derivation of $E_a^{WLF}$ , $\sigma^{RBLM}$ , $E_a^{RBLM}$ , $\sigma^{GS}$ , and $E_a^{GS}$ models

Carella *et al.* reported WLF parameters for various PBs with varying 1,2-addition content.  $T_g$  increased with increasing 1,2-addition content from  $-97$  to  $85$  °C. From linear rheology measurements, they determined that the horizontal shift factors for PB ( $a_T$ ) followed a modified form of the WLF equation

$$\log_{10} a_T(T) = \frac{-C_1(T - T_g - 55 \text{ K})}{C_2 + (T - T_g - 55 \text{ K})} \quad (\text{S9})$$

where  $C_1 = 5.78$  and  $C_2 = 94.8$  K are the WLF parameters for PB homopolymer.<sup>S8</sup> At any temperature, the “instantaneous”  $E_a^{WLF}$  may be obtained by taking the derivative of Eqn. S9<sup>S9</sup>

$$E_a^{WLF} = -2.303RT^2 \frac{\partial \log_{10} a_T}{\partial T} = \frac{2.303C_1C_2RT^2}{(C_2 + T - T_g - 55\text{K})^2} \quad (\text{S10})$$

Evaluating Eqn. S9 at  $T = T_R = 391.15$  K produces Eqn. 8 in the main manuscript.

The Renormalized Bond Lifetime Model (RBLM) describes  $\tau_{XL}$  as

$$\tau_{XL} = Z\tau_b + \tau_{open} \quad (\text{S11})$$

$$\tau_b = \tau_0 \exp\left(\frac{E_a^{sm}}{RT}\right) \quad (\text{S12})$$

where  $\tau_b$  is the Arrhenius model for the bare bond lifetime,  $\tau_0$  is the elementary Rouse timescale,  $Z$  is the number of times a cross-linkable group reassociates with an old partner, and  $\tau_{open}$  is the time it takes for a cross-linkable group to traverse to a new partner. Assuming Rouse subdiffusive motion for cross-links,  $Z$  and  $\tau_{open}$  are estimated by

$$Z = \frac{r_x}{b} \quad (\text{S13})$$

$$\tau_{open} = \tau_0 \left(\frac{r_x}{b}\right)^4 = \tau_0 Z^4 \quad (\text{S14})$$

$$r_x = (c_x)^{-1/3} = \left(\frac{N_{XL}}{b^3 N_n}\right)^{-1/3} \quad (\text{S15})$$

where  $r_x$  is the average distance between cross-linkable groups,  $c_x$  is the number density of cross-links within the network, and  $b = 0.96$  nm is the PB statistical segment length.<sup>S10,S11</sup>  $\sigma^{RBLM}$  may be expressed by

$$\tau_{XL} = Z\tau_b + \tau_{open} = Z\tau_0 \exp\left(\frac{E_a^{sm}}{RT}\right) + \tau_0 Z^4 \quad (\text{S16})$$

$$\tau_{XL} = \left( Z \left( 1 + Z^3 \exp\left(-\frac{E_a^{sm}}{RT}\right) \right) \right) \tau_0 \exp\left(\frac{E_a^{sm}}{RT}\right) = \sigma^{RBLM} \tau_0 \exp\left(\frac{E_a^{sm}}{RT}\right) \quad (\text{S17})$$

$$\sigma^{RBLM} = Z \left( 1 + Z^3 \exp\left(-\frac{E_a^{sm}}{RT}\right) \right) \quad (\text{S18})$$

$E_a^{RBLM}$  may be derived by

$$\ln \tau_{XL} = \ln \tau_0 + \ln \left( \frac{Z\tau_b}{\tau_0} + \frac{\tau_{open}}{\tau_0} \right) = \ln \tau_0 + \ln \left( \frac{Z\tau_b}{\tau_0} + Z^4 \right) \quad (\text{S19})$$

$$E_a^{RBLM} = \frac{\partial}{\partial \left(\frac{1}{RT}\right)} \ln \tau_0 + \frac{\partial}{\partial \left(\frac{1}{RT}\right)} \ln \left( \frac{Z\tau_b}{\tau_0} + Z^4 \right) \quad (S20)$$

$$E_a^{RBLM} = E_a^{WLF} + \frac{\partial}{\partial \left(\frac{1}{RT}\right)} \ln \left( Z \exp \left( \frac{E_a^{sm}}{RT} \right) + Z^4 \right) \quad (S21)$$

$$E_a^{RBLM} = E_a^{WLF} + \frac{Z \exp \left( \frac{E_a^{sm}}{RT} \right) E_a^{sm}}{Z \exp \left( \frac{E_a^{sm}}{RT} \right) + Z^4} \quad (S22)$$

$$E_a^{RBLM} = E_a^{WLF} + \frac{E_a^{sm}}{1 + Z^3 \exp \left( \frac{-E_a^{sm}}{RT} \right)} \quad (S23)$$

where Eqn. 12 from the main manuscript is used to go from Eqn. S20 to S21.

In the theory of Ghosh and Schweizer,  $\tau_b$  is described as

$$\frac{\tau_b}{\tau} = \frac{\tau_0}{\tau} + \left( \frac{\tau_0}{\tau} \right)^{\nu} \exp \left( \frac{\Delta F}{RT} \right) \quad (S24)$$

where  $\nu$  is a decoupling exponent,  $\Delta F$  is the effective association free energy barrier, and  $\tau$  is the elementary attempt time for activated relaxation.<sup>S12</sup> Replacing  $\Delta F$  with  $E_a^{sm}$ , we derive  $\sigma^{GS}$  by substituting Eqn. 24 into the following relationship

$$\tau_{XL} = Z\tau_b + \tau_{open} = Z \left( \tau_0 + \frac{\tau_0^{\nu}}{\tau^{\nu-1}} \exp \left( \frac{E_a^{sm}}{RT} \right) \right) + \tau_0 Z^4 = \sigma^{GS} \tau_0 \exp \left( \frac{E_a^{sm}}{RT} \right) \quad (S24)$$

$$\sigma^{GS} = \frac{Z \left( 1 + \left( \frac{\tau_0}{\tau} \right)^{\nu-1} \exp \left( \frac{E_a^{sm}}{RT} \right) \right) + Z^4}{\exp \left( \frac{E_a^{sm}}{RT} \right)} = Z \left( \left( \frac{\tau_0}{\tau} \right)^{\nu-1} + (1 + Z^3) \exp \left( -\frac{E_a^{sm}}{RT} \right) \right) \quad (S25)$$

$E_a^{GS}$  may be derived by

$$E_a^{GS} = \frac{\partial}{\partial \left(\frac{1}{RT}\right)} \ln \tau_0 + \frac{\partial}{\partial \left(\frac{1}{RT}\right)} \ln \left( \frac{Z\tau_b}{\tau_0} + Z^4 \right) = E_a^{WLF} + \frac{Z \frac{\partial}{\partial \left(\frac{1}{RT}\right)} \left( \frac{\tau_b}{\tau_0} \right)}{\frac{Z\tau_b}{\tau_0} + Z^4} \quad (\text{S26})$$

$$E_a^{GS} = E_a^{WLF} + \frac{Z \frac{\partial}{\partial \left(\frac{1}{RT}\right)} \left( 1 + \tau^{1-\nu} \tau_0^{\nu-1} \exp \left( \frac{E_a^{sm}}{RT} \right) \right)}{Z \left( 1 + \tau^{1-\nu} \tau_0^{\nu-1} \exp \left( \frac{E_a^{sm}}{RT} \right) \right) + Z^4} \quad (\text{S27})$$

$$E_a^{GS} = E_a^{WLF} + \frac{Z\tau^{1-\nu} \left( \tau_0^{\nu-1} \exp \left( \frac{E_a^{sm}}{RT} \right) E_a^{sm} + \exp \left( \frac{E_a^{sm}}{RT} \right) (\nu - 1) \tau_0^{\nu-2} \frac{\partial \tau_0}{\partial \left(\frac{1}{RT}\right)} \right)}{Z \left( 1 + \tau^{1-\nu} \tau_0^{\nu-1} \exp \left( \frac{E_a^{sm}}{RT} \right) \right) + Z^4} \quad (\text{S28})$$

$$E_a^{GS} = E_a^{WLF} + \frac{Z\tau^{1-\nu} \tau_0^{\nu-1} \exp \left( \frac{E_a^{sm}}{RT} \right) (\tau_0^{\nu-1} E_a^{sm} + (\nu - 1) E_a^{WLF})}{Z \left( 1 + \tau^{1-\nu} \tau_0^{\nu-1} \exp \left( \frac{E_a^{sm}}{RT} \right) \right) + Z^4} \quad (\text{S29})$$

$$E_a^{GS} = E_a^{WLF} + \frac{\tau_0^{\nu-1} E_a^{sm} + (\nu - 1) E_a^{WLF}}{1 + \frac{1 + Z^3}{\tau^{1-\nu} \tau_0^{\nu-1} \exp \left( \frac{E_a^{sm}}{RT} \right)}} \quad (\text{S30})$$

where, once again, Eqn. 12 from the main manuscript is invoked in Eqns. S26 and S29.

To produce  $E_a^{RBLM}$  and  $E_a^{GS}$  predictions in Figure 6 of the main manuscript,  $N_{XL}$  as a function of  $T_g$  was estimated using Eqn. 5 of the main manuscript. For  $E_a^{GS}$ ,  $\tau = 1 \times 10^{-12}$  s and  $\nu = 0.66$  were used.<sup>S13</sup>

## References

- <sup>1</sup>Nallasamy, P.; Anbarasan, P. M.; Mohan, S. Vibrational Spectra and Assignments of Cis- and Trans-1,4-Polybutadiene. *Turk J Chem* **2002**, *26*, 105–111.
- <sup>2</sup>Sigma-Aldrich. ATR-IR spectrum of benzyl mercaptan. <https://www.sigmaaldrich.com/deepweb/assets/sigmaaldrich/quality/spectra/863/770/ATIR0016130.pdf> (accessed April 9, 2023)
- <sup>3</sup>Ricarte, R. G.; Tournilhac, F.; Leibler, L. Phase Separation and Self-Assembly in Vitrimers: Hierarchical Morphology of Molten and Semicrystalline Polyethylene/Dioxaborolane Maleimide Systems. *Macromolecules* **2019**, *52*, 432–443. <https://doi.org/10.1021/acs.macromol.8b02144>.
- <sup>4</sup>Chen, Q.; Zhang, Z.; Colby, R. H. Viscoelasticity of Entangled Random Polystyrene Ionomers. *J Rheol* **2016**, *60*, 1031–1040. <https://doi.org/10.1122/1.4955432>.
- <sup>5</sup>Soussou, J. E.; Moavenzadeh, F.; Gradowczyk, M. H. Application of Prony Series to Linear Viscoelasticity. *T Soc Rheol* **1970**, *14*, 573–584. <https://doi.org/10.1122/1.549179>.
- <sup>6</sup>Macosko, C.W. *Rheology: Principles, Measurements, and Applications*, 1st ed.; Wiley-VCH, 1994.
- <sup>7</sup>Wu, S.; Yang, H.; Xu, W.-S.; Chen, Q. Thermodynamics and Reaction Kinetics of Symmetric Vitrimers Based on Dioxaborolane Metathesis. *Macromolecules* **2021**, *54*, 6799–6809. <https://doi.org/10.1021/acs.macromol.1c00697>.
- <sup>8</sup>Carella, J. M.; Graessley, W. W.; Fetters, L. J. Effects of Chain Microstructure on the Viscoelastic Properties of Linear Polymer Melts: Polybutadienes and Hydrogenated Polybutadienes. *Macromolecules* **1984**, *17*, 2775–2786. <https://doi.org/10.1021/ma00142a059>.
- <sup>9</sup>Ferry, J. *Viscoelastic Properties of Polymers*, 3<sup>rd</sup> ed.; John Wiley & Sons Inc, 1980.
- <sup>10</sup>Shanbhag, S.; Ricarte, R. G. On the Effective Lifetime of Reversible Bonds in Transient Networks. *Macromol Theory Simul* **2023**. <https://doi.org/10.1002/mats.202300002>.
- <sup>11</sup>Rubinstein, M.; Colby, R.H. *Polymer Physics*, 1<sup>st</sup> ed.; Oxford University Press, 2003.
- <sup>12</sup>Ghosh, A.; Schweizer, K. S. Physical Bond Breaking in Associating Copolymer Liquids. *ACS Macro Lett* **2021**, *10*, 122–128. <https://doi.org/10.1021/acsmacrolett.0c00697>.
- <sup>13</sup>Soman, B.; Schweizer, K. S.; Evans, C. M. Fragile Glass Formation and Non-Arrhenius Upturns in Ethylene Vitrimers Revealed by Dielectric Spectroscopy. *Macromolecules* **2023**, *56*, 166–176. <https://doi.org/10.1021/acs.macromol.2c01657>.